

# 14-3-3 Coordinates Microtubules, Rac, and Myosin II to Control Cell Mechanics and Cytokinesis

Qiongqiong Zhou,<sup>1</sup> Yee-Seir Kee,<sup>1</sup> Christopher C. Poirier,<sup>3</sup> Christine Jelinek,<sup>2</sup> Jonathan Osborne,<sup>1</sup> Srikanth Divi,<sup>1</sup> Alexandra Surcel,<sup>1</sup> Marie E. Will,<sup>1</sup> Ulrike S. Eggert,<sup>5</sup> Annette Müller-Taubenberger,<sup>6</sup> Pablo A. Iglesias,<sup>3</sup> Robert J. Cotter,<sup>2</sup> and Douglas N. Robinson<sup>1,2,4,\*</sup>

<sup>1</sup>Department of Cell Biology

<sup>2</sup>Department of Pharmacology and Molecular Sciences  
Johns Hopkins University School of Medicine, Baltimore, MD 21205, USA

<sup>3</sup>Department of Electrical and Computer Engineering

<sup>4</sup>Department of Chemical and Biomolecular Engineering  
Johns Hopkins University, Baltimore, MD 21218, USA

<sup>5</sup>Dana Farber Cancer Institute and Department of Biological Chemistry and Molecular Pharmacology, Harvard Medical School, Boston, MA 02115, USA

<sup>6</sup>Institute for Anatomy and Cell Biology,  
Ludwig-Maximilians-Universität München, 80336 Munich, Germany

## Summary

**Background:** During cytokinesis, regulatory signals are presumed to emanate from the mitotic spindle. However, what these signals are and how they lead to the spatiotemporal changes in the cortex structure, mechanics, and regional contractility are not well understood in any system.

**Results:** To investigate pathways that link the microtubule network to the cortical changes that promote cytokinesis, we used chemical genetics in *Dictyostelium* to identify genetic suppressors of nocodazole, a microtubule depolymerizer. We identified 14-3-3 and found that it is enriched in the cortex, helps maintain steady-state microtubule length, contributes to normal cortical tension, modulates actin wave formation, and controls the symmetry and kinetics of cleavage furrow contractility during cytokinesis. Furthermore, 14-3-3 acts downstream of a Rac small GTPase (RacE), associates with myosin II heavy chain, and is needed to promote myosin II bipolar thick filament remodeling.

**Conclusions:** 14-3-3 connects microtubules, Rac, and myosin II to control several aspects of cortical dynamics, mechanics, and cytokinesis cell shape change. Furthermore, 14-3-3 interacts directly with myosin II heavy chain to promote bipolar thick filament remodeling and distribution. Overall, 14-3-3 appears to integrate several critical cytoskeletal elements that drive two important processes—cytokinesis cell shape change and cell mechanics.

## Introduction

Cytokinesis is driven by regional mechanical activities—myosin II-based contractility, actin polymer dynamics, and actin crosslinking. Over the years, we have discovered and have been studying a two-component system of equatorial and global/polar actin-associated proteins that govern these

dynamical and mechanical features of the dividing cell cortex. The global pathway is controlled by a Rac-family small GTPase (encoded by the *RacE* gene), which regulates the distribution of cortical actin crosslinkers and provides resistive stresses to modulate furrow ingression kinetics [1–3]. Although active cell shape change is ultimately driven and controlled by these cortical mechanical features, the process is regulated spatially and temporally by the mitotic spindle.

The mitotic spindle has two major structures—the central spindle and the astral microtubule network—that regulate the cortex (e.g., [4–6]); however, the molecular bases of these signaling cascades are not well defined. The central spindle signals are mediated partly by kinesin-6-family motors complexed with two general sets of proteins, including MgcRac-Gap (in metazoans) or the chromosomal passenger proteins INCENP and Aurora kinase (in *Dictyostelium* protozoans and metazoans) [7–10]. The astral microtubules play an important role in many cell types, including *Dictyostelium*, echinoderms, and *C. elegans* embryos where they help direct symmetry breaking [4, 11, 12]. The major signaling pathway activated by these astral microtubules has remained largely elusive, though a heterotrimeric G protein pathway has been implicated in some systems (e.g., [13]). Yet, *Dictyostelium* G $\beta$  null mutants (*Dictyostelium* G $\beta$  is encoded by a single gene) are primarily defective in chemotaxis-assisted scission [14]. Overall, significant gaps remain in our understanding of how the mitotic spindle regulates the regional mechanics that drive cytokinesis cell shape change.

Here, we used nocodazole to disturb microtubules and searched for genes involved in microtubule-related regulatory pathways via cDNA library suppression analysis. Using this chemical-genetic approach, we identified 14-3-3 overexpression as a genetic suppressor of nocodazole. The 14-3-3 proteins are a family of abundant proteins that are widely expressed in all eukaryotic cells and are highly conserved from *Dictyostelium* to mammals. 14-3-3 has been implicated in cytokinesis completion, and the mammalian isoform 14-3-3 $\sigma$  is involved in mitotic translational control [15, 16]. Two isoforms are found in yeast, *Drosophila*, and *C. elegans*. *Dictyostelium* cells have only one isoform, which makes *Dictyostelium* a unique system for 14-3-3 studies. Here, we present evidence that 14-3-3 functions in a pathway linking microtubules, RacE, and myosin II to cortex mechanics, cortical actin wave dynamics, and cytokinesis shape control.

## Results

### 14-3-3 Is a Genetic Suppressor of Nocodazole

To begin dissecting how the mitotic spindle modulates cytokinesis, we challenged pools of cDNA library transformed cells with nocodazole at IC<sub>50</sub>, the concentration that reduced the growth rate by 50% (measured to be 10  $\mu$ M). From 100 pools of 1,000 cDNA library transformants (100,000 total transformants), we recovered 14-3-3 (see sequence analysis in Figure S1 available online) and a dominant-negative version of enlazin (enl-tr), the *Dictyostelium* ezrin-radixin-moesin (ERM)-family protein [17]. Both 14-3-3 and enl-tr recapitulated the nocodazole suppression (Figure 1A), verifying the genetic

\*Correspondence: dnr@jhmi.edu

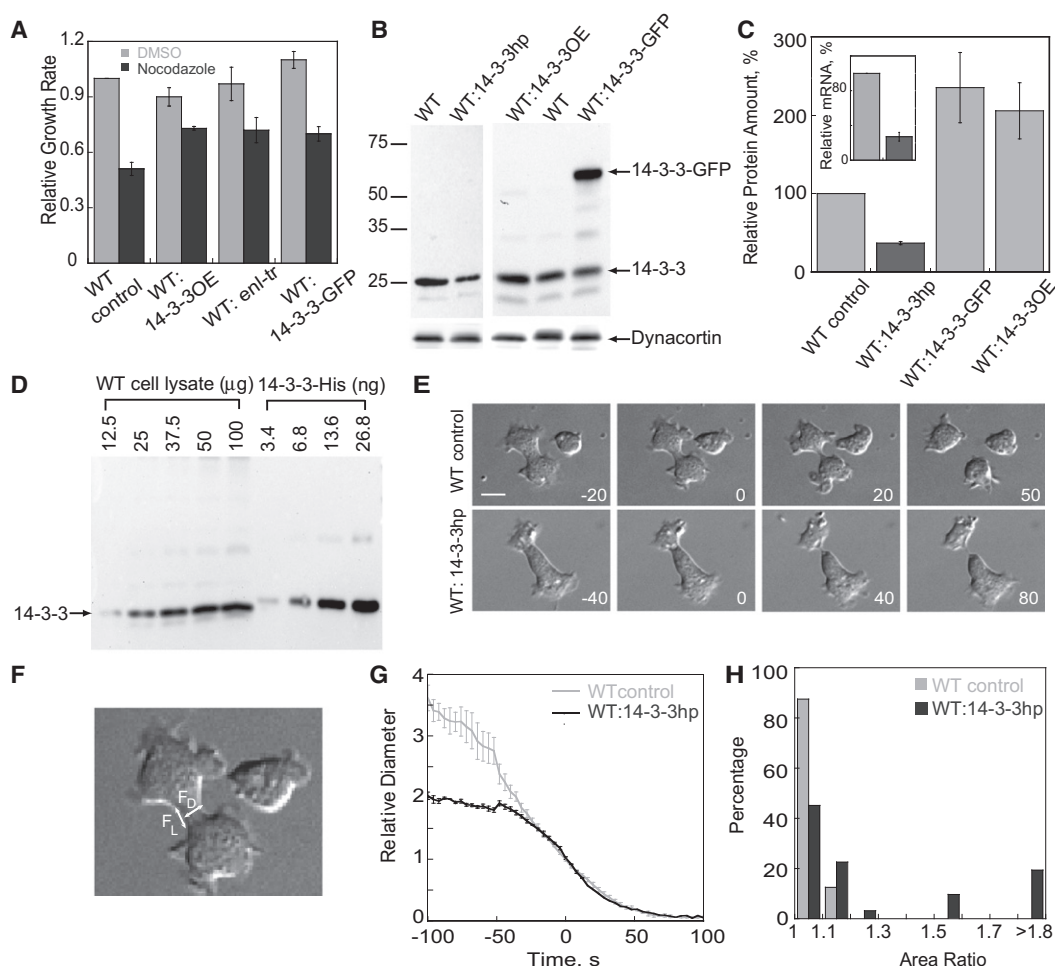


**Figure 1. Overexpression of 14-3-3 Rescues Nocodazole Inhibition, and Downregulation of 14-3-3 Introduces a Cytokinesis Defect**

(A) Expression of 14-3-3OE, a dominant-negative version of enlazin (enl-tr), or 14-3-3-GFP recapitulates rescue of nocodazole inhibition (two-tailed Student's *t* test [ST]:  $p < 0.05$ ,  $n \geq 5$  for each condition). Control cells carried the empty vector. Cells were challenged with 10  $\mu$ M nocodazole ( $IC_{50}$ ) or dimethyl sulfoxide (DMSO).

(B) Western analysis showing the expression levels of 14-3-3 in wild-type (WT), WT:14-3-3hp, WT:14-3-3OE, and WT:14-3-3-GFP cells. Dynacortin provides a loading control.

(C) Quantification of 14-3-3 protein amounts in WT control (100%), WT:14-3-3hp (37%), WT:14-3-3-GFP (240%), and WT:14-3-3OE (210%) cells ( $n = 4$ ). Inset shows real-time reverse transcriptase-polymerase chain reaction result of knockdown of 14-3-3 mRNA in 14-3-3hp cells (level was 27% of control;  $n = 4$ ).

(D) Quantitative western analysis showing absolute 14-3-3 protein amount in WT cells. Dilution series of total cell lysate and purified 14-3-3-His protein were compared.

(E) Differential interference contrast (DIC) time series of a WT control cell (top) and a WT:14-3-3hp cell (bottom) undergoing cytokinesis. Scale bar represents 10  $\mu$ m.

(F) Time 0 in (E) was defined as the point when the furrow diameter reached  $D_x$  ( $D_x$  is the point when the furrow diameter ( $F_D$ ) equaled the furrow length ( $F_L$ ) as shown here).

(G) Rescaled furrow-thinning trajectories for WT control ( $D_x = 2.8 \pm 0.08$ ;  $n = 14$ ) and WT:14-3-3hp ( $D_x = 2.6 \pm 0.09$ ;  $n = 15$ ) cells.

(H) Graph showing the distribution of two daughter cells' 2D-projected area ratio (larger area/smaller area). WT control cells are distributed from 1.0 to 1.2 ( $n = 20$ ), whereas WT:14-3-3hp cells are distributed from 1.0 to 2.8 (1.8–2.8 are grouped in the histogram) ( $n = 31$ ). These distributions are significantly different (Mann-Whitney nonparametric test [MW]:  $p = 0.004$ ).

Error bars represent standard error of the mean (SEM).

interactions with nocodazole. Because enl-tr was originally identified as a genetic suppressor of *cortexillin-1* mutants [17], the recovery of 14-3-3 and enl-tr in this genetic selection led us to ask whether 14-3-3 links the microtubule network to the actin cortex to modulate cytokinesis contractility.

To initiate characterization of 14-3-3, we purified a recombinant His-tagged 14-3-3 and generated polyclonal antibodies. In the 14-3-3 overexpression cell-lines, 14-3-3 levels were increased approximately 2-fold relative to control cells (Figures 1B and 1C). We also quantified the wild-type (WT)

cellular concentration of 14-3-3, which was 1.4  $\mu$ M monomer, corresponding to a 0.7  $\mu$ M dimer (the typical functional unit of 14-3-3) concentration (Figure 1D). This concentration is similar to that found for other actin-associated proteins, including dynacortin (1  $\mu$ M) [18], fimbrin (0.6  $\mu$ M) [19], and myosin II (3.4  $\mu$ M) [20].

#### Downregulation of 14-3-3 Induces Cytokinesis Defects

We attempted to delete 14-3-3 by homologous recombination. However, this effort yielded highly enlarged, fragile cells

(typical of multinucleated cells with a severe cortical defect), which died within a few generations (Figures S2A–S2C). Therefore, we downregulated 14-3-3 expression levels by using a hairpin construct (14-3-3hp). Our data confirmed that 14-3-3 is an essential gene: complete silencing by the hairpin similarly killed the cells under standard drug conditions. However, we established a protocol for achieving partial RNA interference (RNAi), allowing the recovery of WT:14-3-3hp cells (WT cells expressing the 14-3-3hp plasmid) with a 60%–70% knockdown of both RNA and protein levels (Figures 1B and 1C). These cells had a slower growth rate in suspension culture (Figure S2D) and a larger overall cell size (Figure S2E) as compared with control cells. DAPI staining revealed that these enlarged 14-3-3hp cells were multinucleated, indicating a cytokinesis defect (Figures S2E and S2F). The 14-3-3 levels were inversely correlated with the degree of multinucleation (severity of the cytokinesis defect) (Figure S2G).

To assess how 14-3-3 contributes to cytokinesis contractility, we quantified the furrow ingression dynamics using our rescaling scheme [2, 3, 17]. In this scheme, wild-type cleavage furrows ingress following a slow, nonlinear trajectory. In contrast, mutants in either the global or equatorial pathways divide following a multiphasic trajectory in which the early stage is slow and the late phase accelerates relative to the initial phase. As compared to wild-type cells, WT:14-3-3hp cells have an altered furrow morphology (Figure 1E) and a multiphasic furrow ingression dynamic (Figures 1F and 1G). The differential interference contrast time-lapse and the rescaled furrow-thinning dynamics show that downregulation of 14-3-3 slows down the initial bridge ingression. Finally, these 14-3-3hp cells also exhibit an elongated bridge length and have a higher probability of asymmetrical division as reflected by the area ratio of the two daughter cells (Figures 1E and 1H). To summarize, 14-3-3 ensures symmetrical cell division and wild-type furrow ingression dynamics. It is worth noting that the morphology and dynamics of the 14-3-3hp cytokinesis are highly reminiscent of *myoII* null cytokinesis [2, 3].

#### 14-3-3 Enriches at the Cell Cortex

Next, we analyzed the subcellular localization of 14-3-3 by immunocytochemistry and by live-cell imaging of cells expressing 14-3-3-GFP. By immunocytochemistry, 14-3-3 was found to be concentrated in the cortex of wild-type and 14-3-3-overexpressing (14-3-3OE) cells but was depleted from the cortex in 14-3-3hp cells (Figure 2A). Similarly, 14-3-3-GFP showed cortical enrichment that was distinct from soluble GFP in live cells (Figure S2H). Mutation (K49E; [21]) of the key conserved lysine in 14-3-3's ligand-binding cleft partially reduced the cortical enrichment of 14-3-3, indicating that the cortical enrichment is dependent on ligand binding (Figure S2H). During cytokinesis, 14-3-3 was enriched in the global/polar cortex in fixed (Figure 2B) and live (Figure S2I) cells. We did not observe clear colocalization of 14-3-3 with microtubules by either method. To ensure that the 14-3-3-GFP was functional, we confirmed its ability to rescue nocodazole treatment, which was similar to that of the untagged version (Figure 1A).

#### 14-3-3 Maintains Steady-State Microtubule Lengths

Because 14-3-3 was recovered as a genetic suppressor of nocodazole, we examined the microtubule structures in control cells and in cells with altered 14-3-3 expression levels with or without nocodazole (Figure 2C). To simplify the analysis, we examined the total microtubule length by epifluorescence

microscopy when cells were flattened with a sheet of agarose (Figure 2C). We found that the average microtubule was ~30% shorter in 14-3-3hp cells, whereas 14-3-3OE did not significantly alter the average microtubule length. Upon nocodazole treatment, the average length decreased from ~10  $\mu\text{m}$  to 2  $\mu\text{m}$  in control cells, whereas 14-3-3OE cells had longer microtubules than the control cells had.

Because 14-3-3 was enriched in the cortex, we sought to determine whether alteration of 14-3-3 levels specifically changed the extent and dynamics of microtubule-cortex interactions. Here, we define the microtubule-cortex interaction site as the region of the microtubule detected by total internal reflection fluorescence microscopy, which only illuminates ~200 nm from the cell-surface interface (Figure S3A). We developed a semiautomated microtubule-tracking algorithm to quantify the microtubule-cortex interaction length and lifetime. We found that the lifetimes of the microtubule-cortex interactions were similar ( $\tau \approx 5$  s) for all genotypes (WT control, WT:14-3-3OE, and WT:14-3-3hp) with or without nocodazole (data not shown). We also analyzed the microtubule-cortex contact length distributions (Figure S3B). We found that without nocodazole, perturbation of 14-3-3 levels significantly altered these distributions, whereas with nocodazole, the data interpretation was complicated by the fact that nocodazole-treated cells were more photosensitive.

Because 14-3-3hp cells had a cytokinesis defect (Figure 1) and an interphase microtubule structural defect (Figure 2C), we needed to determine whether there was a defect in mitotic spindle-associated microtubules. However, it is difficult to detect all astral microtubules making contact with the cortex. Instead, we analyzed the mitotic spindle dynamics, specifically the spindle length change and angular velocity. We could not find any quantitative impact on the mitotic spindle dynamics upon 14-3-3 depletion (Figure S3C).

The cortical localization of 14-3-3 led us to test whether it is involved in cortical mechanics. We measured effective cortical tension via micropipette aspiration. When wild-type cells were treated with nocodazole (10  $\mu\text{M}$ ), the cortical tension was reduced by 60% (Figure 2D). Overexpression of 14-3-3 partially rescued the cortical tension defect of nocodazole-treated cells (raising it from 0.4 to 0.8 nN/ $\mu\text{m}$ ; Figure 2D). In contrast, 14-3-3hp cells had a 40% reduction in interphase cortical tension (Figure 2E), and expression of the ligand-binding mutant 14-3-3(K49E) had a dominant-negative effect on cortical tension, reducing it by 30% compared to WT control (Figure 2F). These observations suggest that 14-3-3 works with microtubules to control cortical mechanics.

#### 14-3-3 Functions Downstream of RacE to Regulate the Cell Cortex and Cytokinesis

RacE is important for cytokinesis, cortical tension, and the cortical accumulation of the global actin crosslinkers dynacortin and coronin [1, 22]. Though dynacortin and coronin are downstream of RacE, the pathways governed by RacE are largely unknown. Because 14-3-3 also controls cortical tension and is globally distributed during cytokinesis, we tested whether 14-3-3 participates in the RacE signaling pathway. 14-3-3-GFP was expressed in *RacE* null cells, and the localization of 14-3-3-GFP was examined. Without RacE, 14-3-3-GFP failed to accumulate in the cortex (Figure 3A). However, when the cells were complemented with mCherry-RacE, the cortical localization of 14-3-3 was restored (Figure 3A). To begin to characterize this RacE dependency of 14-3-3's cortical localization, we tested 14-3-3's solubility.

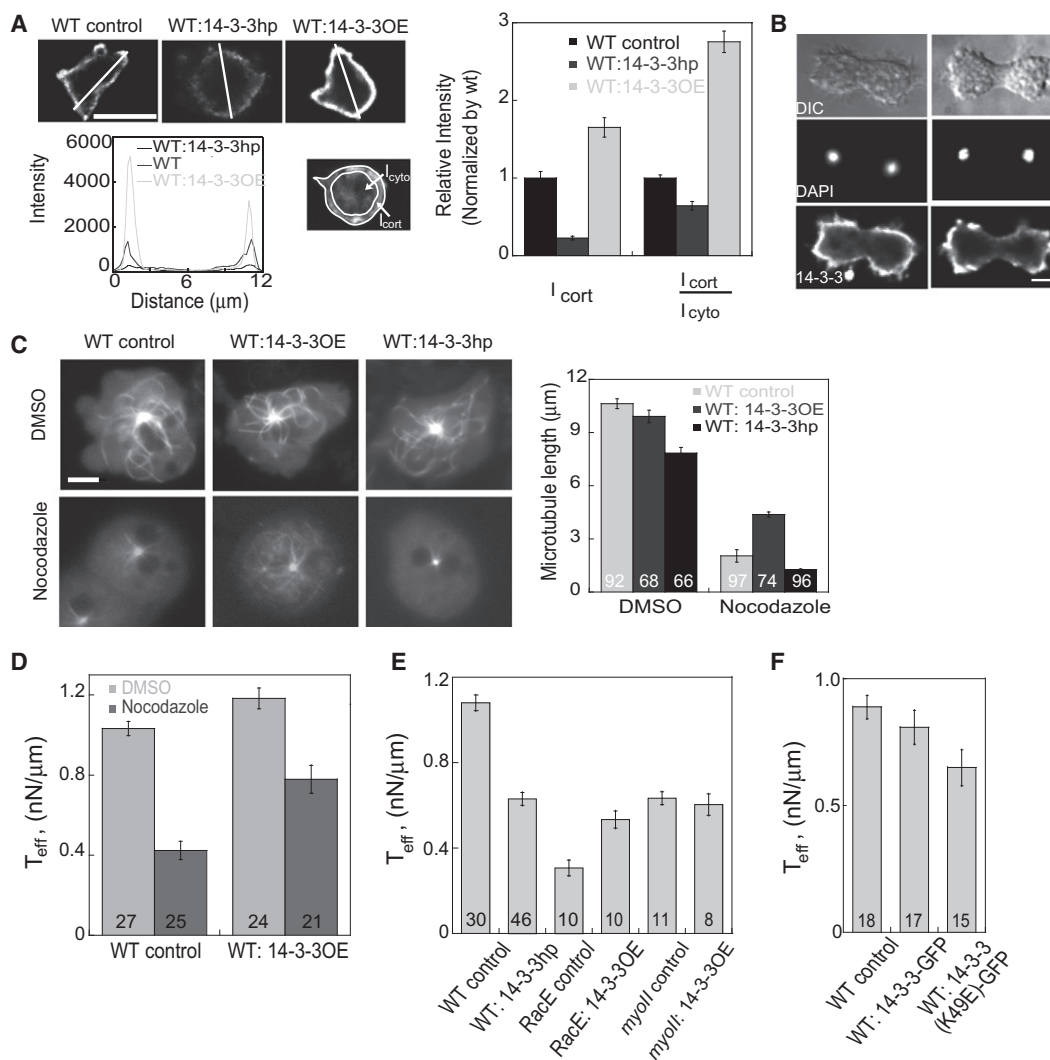


**Figure 2. Cortically Enriched 14-3-3 Contributes to Cortical Mechanics and Microtubule Length**

(A) Anti-14-3-3 immunocytochemistry of WT control, WT:14-3-3hp, and WT:14-3-3OE cells shows that 14-3-3 is enriched in the cortex. Line scan shows the two peaks of 14-3-3 signal on the cell edges. Cartoon shows the method of quantifying the ratio of intensities of the cortex to cytoplasm. Histogram shows the relative intensity ( $I_{\text{cort}}$ ) and the cortex/cytoplasm intensity ratios ( $I_{\text{cort}}/I_{\text{cyto}}$ ) from fixed-cell imaging ( $n = 10$  cells for each strain). For both parameters, 14-3-3 levels of 14-3-3hp and 14-3-3OE are significantly different from control (ST:  $p < 0.001$ ). Error bars represent SEM.

(B) Two examples of fixed dividing wild-type cells stained with DAPI and anti-14-3-3 antibody, showing that 14-3-3 is enriched at the cortex but diminished in the cleavage furrow cortex.

(C) Whole microtubules were visualized by epifluorescence after the cells were flattened by a slice of agarose. GFP-tubulin-labeled WT control, WT:14-3-3OE, and WT:14-3-3hp cells were treated with DMSO or  $10 \mu\text{M}$  nocodazole for 30 min before imaging. Graph shows the total microtubule length of WT control, WT:14-3-3OE, and WT:14-3-3hp cells without (DMSO) or with nocodazole treatment. Total microtubule length is much shorter in WT:14-3-3hp cells compared to WT control cells (ST:  $p < 0.0001$ ). Nocodazole treatment significantly shortened the total length of microtubules in all three strains, but 14-3-3OE cells had a significantly longer total microtubule length in nocodazole (ST:  $p < 0.0001$ ).

(D–F) Quantification of effective cortical tension measurements by micropipette aspiration.

(D) Nocodazole treatment ( $5 \mu\text{M}$  for 30 min) significantly reduced the effective cortical tension of wild-type cells from  $1.0$  to  $0.42 \text{ nN}/\mu\text{m}$  (ST:  $p < 0.0001$ ), and overexpression of 14-3-3 partially rescued the cortical tension to  $0.78 \text{ nN}/\mu\text{m}$  (ST:  $p < 0.001$ ).

(E) The effective cortical tension was significantly reduced in WT:14-3-3hp cells from  $1.1$  to  $0.63 \text{ nN}/\mu\text{m}$  (ST:  $p < 0.0001$ ). 14-3-3OE raised *RacE* mutant cortical tension from  $0.31$  to  $0.54 \text{ nN}/\mu\text{m}$  (ST:  $p < 0.001$ ). 14-3-3OE did not affect the cortical tension of *myoII* null cells.

(F) Expression of 14-3-3(K49E)-GFP reduced cortical tension by 30% as compared to WT control cells (ST:  $p = 0.009$ ).

Values plotted in (C)–(F) are mean  $\pm$  SEM, with sample sizes listed on the bars.

We lysed cells with 0.1% NP-40 and found that a greater fraction ( $\sim 30\%$  versus less than  $\sim 10\%$ ) of 14-3-3 sedimented in the pellet fraction when *RacE* was expressed in the cell and GTP was provided in the lysis buffer (Figure 3B). Stronger detergents such as 0.1% Triton X-100 disrupted this GTP- and *RacE*-dependent fraction, suggesting that the insoluble fraction has a membrane component rather than being purely

cytoskeleton associated. Furthermore, overexpression of 14-3-3 partially rescued the cortical tension defect in *RacE* null cells (Figure 2E). *RacE* null cells have a cortical tension that is 30% of wild-type, but when 14-3-3 is overexpressed, the cortical tension was nearly doubled to 55% of wild-type. Together, these findings suggest that 14-3-3 participates in the signaling pathway from *RacE* to the cortical



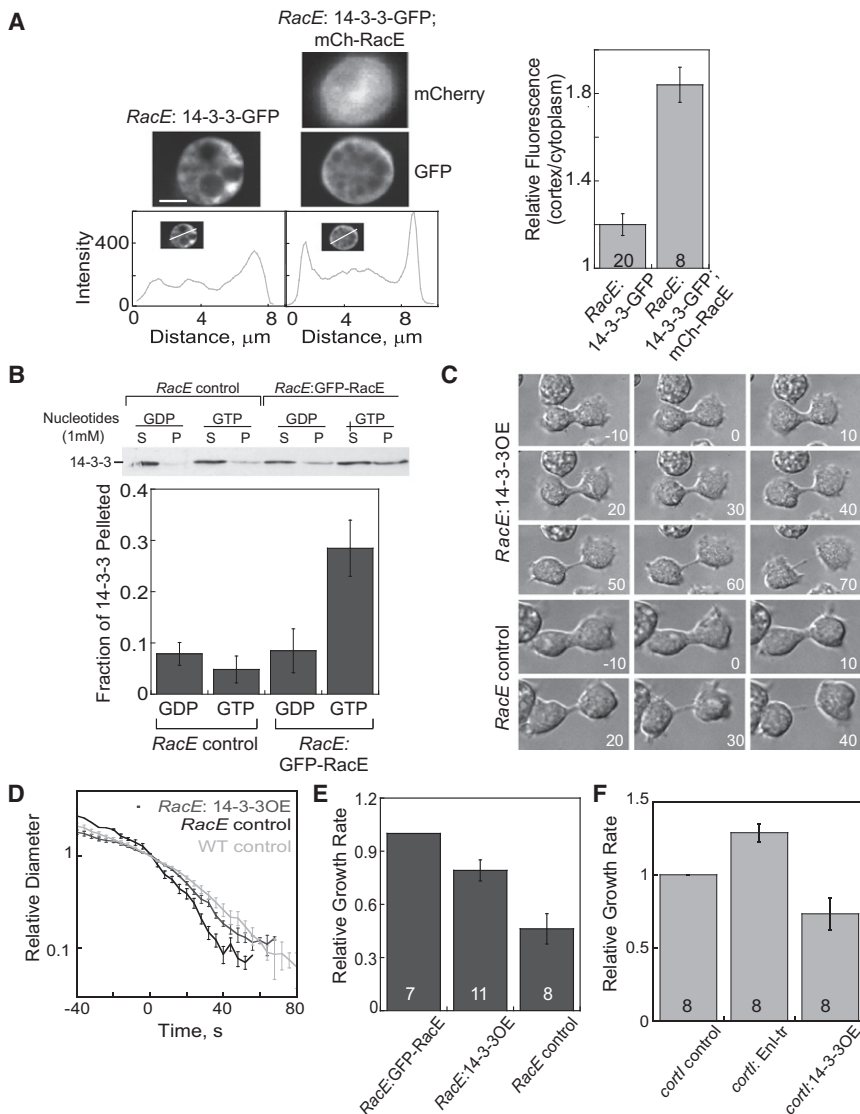


Figure 3. 14-3-3 Depends on RacE for Cortical Localization, and 14-3-3OE Partially Rescues *RacE* Cytokinesis

(A) 3D deconvolution of *RacE* null (left) or mCherry-RacE-rescued *RacE* (right) cells expressing 14-3-3-GFP. Line scans show the cortical 14-3-3 levels. The histogram at right shows quantification of cortical 14-3-3 relative to the cytoplasm in *RacE* null and rescued *RacE* cells. The samples are significantly different from each other (ST:  $p < 0.0001$ ).

(B) Increased separation of 14-3-3 into the insoluble (pellet) fraction (P) from *RacE*:GFP-RacE lysates supplemented with GTP. Addition of GDP or preparation of lysates from *RacE* null cells caused 90% of the 14-3-3 to fractionate in the supernatant fraction (S). Equivalent volumes were loaded in each lane. The histogram at bottom shows the quantification of the fraction of 14-3-3 pelleted ( $n = 3$  for each condition); the amount of 14-3-3 found in the pellet fraction in the *RacE*:GFP-RacE + GTP sample was significantly greater than the other samples (ST:  $p < 0.05$  for each comparison).

(C) DIC time series showing dividing *RacE*:14-3-3OE and *RacE* control cells. Time 0 is the time point when the relative diameter (rescaled by  $D_0$ ) equals 1.

(D) Rescaled furrow-thinning trajectories of *RacE*:14-3-3OE ( $n = 8$ ), *RacE* control ( $n = 20$ ), and WT ( $n = 14$ ) cells show that *RacE*:14-3-3OE furrow ingression dynamics are more similar to WT cells than *RacE* control cells.

(E) Relative growth rates of *RacE*:GFP-RacE, *RacE*:14-3-3OE, and *RacE* control cells. Both *RacE*:GFP-RacE and *RacE*:14-3-3OE grow significantly more quickly than *RacE* control (ST:  $p < 0.01$  in both cases).

(F) Relative growth rates of *cort*:*Enl-tr*, and *cort*:14-3-3OE cells. 14-3-3 was unable to rescue *cort* cells, whereas *Enl-tr* partially rescued *cort* mutants (ST:  $p < 0.001$ ). Error bars represent SEM, with sample sizes listed on the bars in (A), (E), and (F).

cytoskeleton: 14-3-3 depends on RacE for its cortical localization and its separation into the NP40-insoluble fraction, and overexpression of 14-3-3 partially rescues the mechanical defect in *RacE* null cells.

Because *RacE* and 14-3-3 mutants have severe mechanical defects, we examined the actin network of these cells. Here, we expressed GFP-tagged LimEΔcoil to identify polymeric actin in wild-type or WT:14-3-3hp cells and discovered that 14-3-3 modulates cortical actin wave formation (Figures S3D–S3H; Table S2). Actin waves are dynamic actin assemblies that form at the cell-substrate interface and propagate along the surface in a manner dependent on Arp2/3 and myosin I, but not myosin II [23]. 14-3-3-GFP itself did not show wave behavior (data not shown). *RacE* mutants also showed a suppressed cortical actin activity in the same assay, though the qualitative features were slightly different in this strain background (data not shown). In combination, these observations indicate that 14-3-3 modulates cortex mechanics downstream of RacE, which may then have an indirect effect on cortical actin wave dynamics.

We next tested whether 14-3-3 could rescue the *RacE* null cytokinesis and suspension growth defects. As compared to

*RacE* null cells, the cytokinesis morphology was qualitatively rescued (Figure 3C) and the furrow ingression dynamics were quantitatively slowed down in *RacE*:14-3-3OE cells, making them more wild-type-like (Figure 3D). Furthermore, 14-3-3 overexpression partially rescued the suspension growth defect of *RacE* null cells (Figure 3E). This genetic suppression is specific to *RacE* null cells, because it failed to suppress *cort* null (Figure 3F), *myoII* null, and *kif12* null cells (*kif12* encodes the *Dictyostelium* kinesin-6-family protein [24]), all of which are cell lines with severe cytokinesis defects in suspension culture (data not shown). Thus, 14-3-3 specifically acts in a pathway that links the microtubule network and RacE and controls cell mechanics and cytokinesis shape progression.

#### 14-3-3 Associates with Myosin II, Regulating Its Distribution and Assembly

To determine how 14-3-3 controls cytokinesis and cortical mechanics, we used high-resolution mass spectrometry to identify novel 14-3-3 binding partners. We expressed a 14-3-3-FLAG protein in cells and isolated associated proteins by anti-FLAG coimmunoprecipitation (Figure S4A).

14-3-3-FLAG-associated proteins were identified by database searching and prioritized via a spectral counting-based protein quantification and statistical analysis strategy (see [Supplemental Experimental Procedures](#)). From this, a list of potential 14-3-3 interactors was assembled ([Figure S4B](#)). As expected, the most abundant protein identified from the anti-FLAG immunoprecipitation was 14-3-3. The third most abundant protein was myosin II heavy chain protein, and other proteins of interest included fimbrin and myosin II heavy chain kinase. Given the roles of 14-3-3 and myosin II in cortical mechanics and cytokinesis, we chose to focus on their interactions first. Using antibodies directed against myosin II heavy chain and 14-3-3, we tested whether endogenous myosin II and 14-3-3 do in fact associate ([Figures 4A and 4B](#)). These endogenous proteins could be reciprocally coimmunoprecipitated (in case the proteins associated indirectly through actin,  $Mg^{2+}$  and ATP were included in the buffers to prevent myosin II from locking onto actin). Using sequence analysis, we found several motif 2 and 3, but no motif 1, consensus 14-3-3 binding sites in the myosin II heavy chain peptide ([Figure S4C](#)). Three of these binding sites overlapped or were adjacent to three critical threonines in the myosin II heavy chain tail that regulate myosin II bipolar thick filament (BTF) assembly [25]. The BTF assembly-incompetent phosphomimic myosin II 3 $\times$ Asp (where the three threonines have been substituted with aspartic acids) failed to coimmunoprecipitate 14-3-3. Therefore, 14-3-3 likely only associates with assembly-competent myosin II.

To determine whether this association is functionally relevant, we examined the distribution of GFP-myosin II (expressed in a *myoII* null background) and found that GFP-myosin II distribution was severely altered in 14-3-3hp cells ([Figure 4C](#)). In particular, myosin II was significantly less uniform, even punctate, in 14-3-3hp cells. During cytokinesis, GFP-myosin II could still accumulate at the furrow but did so in a highly aggregated fashion ([Figure 4C](#)). In contrast, 14-3-3 overexpression did not appear to alter the wild-type GFP-myosin II distribution ([Figure 4C](#)). Finally, 14-3-3 required myosin II in order to accumulate in the cortex (data not shown).

To determine how 14-3-3 impacts BTF assembly dynamics, we performed fluorescence recovery after photobleaching (FRAP) analysis of GFP-myosin II in the cleavage furrow and interphase cortices ([Figure 4D](#); [Figure S4D](#)). For all genotypes (WT control, WT:14-3-3OE, and WT:14-3-3hp), GFP-myosin II had a recovery time ( $\tau_{rec}$ ) of 3–5 s in interphase and cleavage furrow cortices. However, the immobile fraction was significantly increased in the 14-3-3hp cells in both the cleavage furrow and the interphase cortex ([Figure 4D](#); [Figure S4D](#)). Overall, we found a general trend in which the immobile fractions increased such that 14-3-3OE < control < 14-3-3hp. These observations indicate that 14-3-3 associates with assembly-competent myosin II, increasing its mobility so that it can remodel along the interphase and cleavage furrow cortices.

To test whether 14-3-3 directly impacts myosin II assembly, we performed BTF assembly assays with purified myosin II from *Dictyostelium* and recombinant *Dictyostelium* 14-3-3-His purified from *E. coli*. BTF assembly is highly salt dependent, with the optimal concentrations for myosin II BTF assembly occurring in the range of 25 to 100 mM NaCl [25]. Using equimolar (250 nM) 14-3-3 dimer and myosin II hexameric monomer (two heavy chains, two regulatory light chains, and two essential light chains), we measured the percentage of soluble myosin II as a function of salt concentration ([Figure 4E](#)). Under these conditions, 20% of the myosin II

remains soluble due to the critical concentration of myosin II in the range of 25–100 mM salt. We found that 14-3-3 increased the fraction of soluble myosin slightly from ~20% to ~30%. This level of soluble myosin II is similar to that measured for the 1 $\times$ Asp and 2 $\times$ Asp mutant myosins, rather than the full 3 $\times$ Asp assembly-incompetent myosin II [26]. We could not detect appreciable increases in the 14-3-3 levels in the insoluble assembled fraction, most likely because 14-3-3 interacts in a highly substoichiometric manner with the myosin II monomers in the BTFs. Synthesizing the in vivo FRAP and in vitro BTF assembly results, 14-3-3 shifts myosin II out of the assembled state in vitro and increases the mobile fraction in vivo in order to allow the myosin II to remodel and redistribute around the cell cortex. Because 14-3-3 promotes myosin II mobility and both proteins contribute to cortical mechanics, we asked whether 14-3-3 required myosin II in order to have an impact on cortical tension. We found that 14-3-3OE did not have an effect on the cortical tension of *myoII* null cells ([Figure 2E](#)). Thus, 14-3-3 works through myosin II to control cortical tension.

## Discussion

Cytokinesis shape change occurs over a fast, five-minute time span, requiring considerable cortical remodeling during this time frame. Much insight has come from studying the myosin heavy chain kinases (MHCK), which phosphorylate the critical threonines in the tail of myosin II heavy chain to control BTF assembly [25, 27]. Most likely, the role of these enzymes is to set the level of the free pool of myosin II monomers (~80%) in the cell. This free pool is then maintained through flux of the assembled and disassembled BTF states and is required to ensure that the contractile network is turned over during processes like motility and cytokinesis. 14-3-3 also impacts this dynamic, preventing the myosin II from forming higher-order assemblies and shifting the assembly equilibrium. Importantly, the cellular concentrations of myosin II in the BTF state and the 14-3-3 dimer are identical (0.7  $\mu$ M), indicating that hypotheses of direct biochemical modulation of BTF assembly by 14-3-3 are reasonable. Four scenarios may be envisioned for how 14-3-3 might modulate BTF dynamics. First, by binding to unphosphorylated monomers, 14-3-3 may suppress myosin II thick filament nucleation and/or elongation so that fewer well-structured BTFs are assembled. Second, 14-3-3 may bind transiently to the mature BTF, lowering individual monomer affinity and helping it to release from the BTF. Third, the in vivo system may be more complex where 14-3-3 binds to the BTF, putting the myosin monomers in a configuration that makes them more ideal substrates for MHCK. Considering that MHCK was identified as a potential 14-3-3 protein interactor in our mass spectrometric analysis, such a tertiary complex of myosin BTF-MHCK-14-3-3 might be formed. Fourth, 14-3-3 might form part of the myosin II BTF cortical receptor/anchoring complex. In no system is it well established how myosin II BTFs are anchored to the cortex. In dividing 14-3-3hp cells, the myosin II aggregates appear to dislodge from the cortex, suggesting that 14-3-3 might contribute to cortical anchoring. Overall, this system is highly dynamic, with all of the measured timescales occurring on the order of low seconds. The data also demonstrate that if myosin II BTFs are not distributed uniformly, they cannot contribute to cortex mechanics, and therefore the 14-3-3hp cortical tension and cytokinesis morphology closely resembles that of *myoII* null cells. These observations may

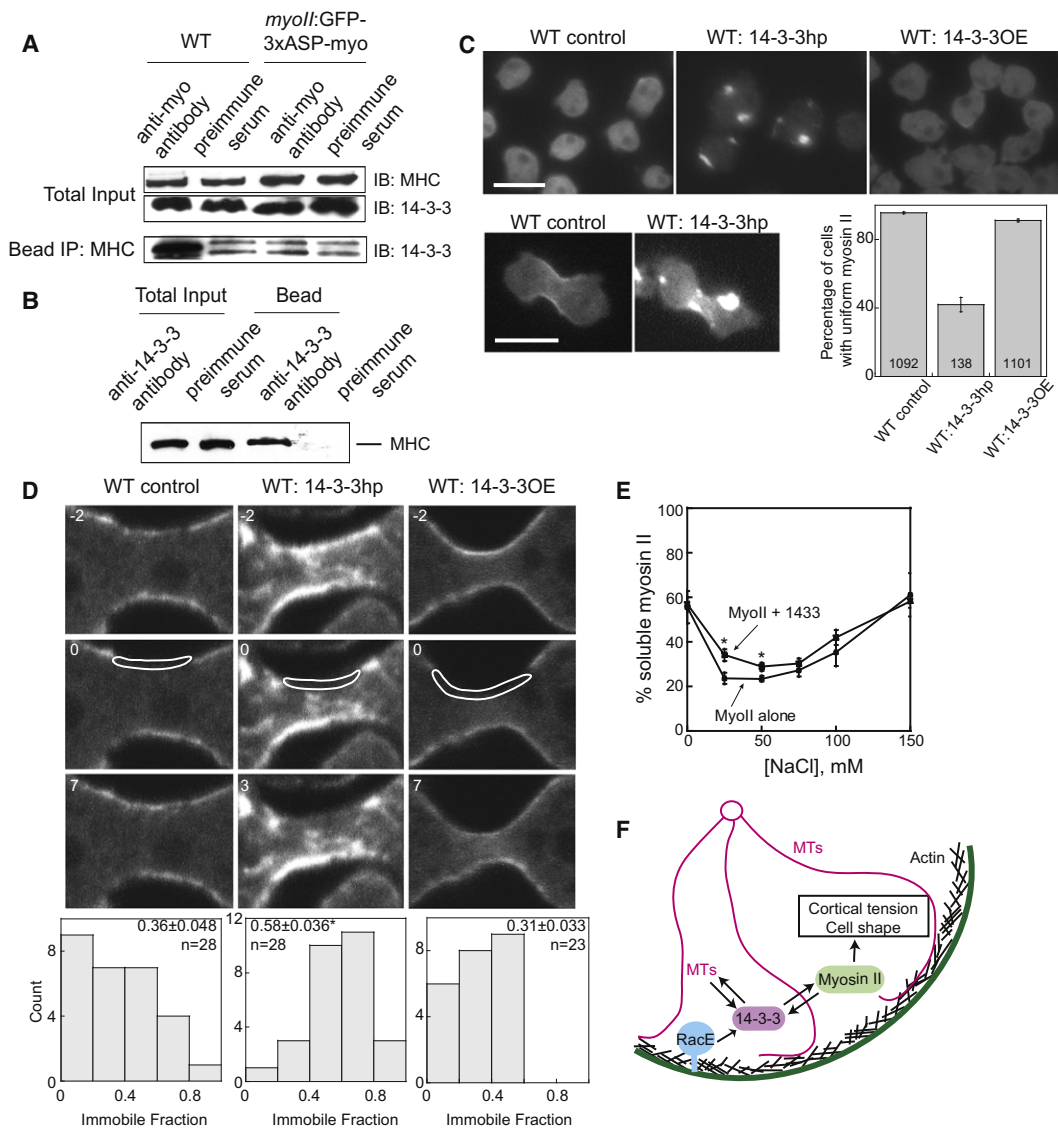


Figure 4. 14-3-3 Associates with Myosin II, Facilitating Myosin II Cortical Remodeling

(A) 14-3-3 coimmunoprecipitates with endogenous WT myosin II, but not with 3×Asp myosin II (bottom panel). Preimmune sera are shown for additional controls. Total input of endogenous and 3×Asp myosin II and 14-3-3 is shown in the top panels. Bead IP refers to the antibody used for the immunoprecipitation; IB refers to the antibody used for the immunoblots. For (A) and (B),  $Mg^{2+}$  and ATP were added to the lysis buffers to ensure that the association did not occur through myosin-actin interactions.

(B) Endogenous myosin II coimmunoprecipitates with endogenous 14-3-3.

(C) GFP-myosin II is more punctate in 14-3-3hp cells, whereas 14-3-3OE does not affect the distribution of GFP-myosin II. During cytokinesis, GFP-myosin II can still localize in the cleavage furrow cortex but is highly punctate. Scale bars represent 10  $\mu$ m and apply to all panels in each group. Histogram shows the percentage of cells with uniform (nonpunctate) GFP-myosin II. The 14-3-3hp cells had a significantly lower fraction of cells with uniform myosin II distribution (comparison of proportions:  $z = 15.6$ ;  $p < 6 \times 10^{-6}$ ). Error bars represent SEM, with sample sizes listed on the bars. For (C) and (D), “WT” cells are *myoII* null cells rescued with wild-type GFP-*myoII*. Control cells carry the empty vector.

(D) As observed from FRAP analysis, 14-3-3hp increases the immobile fraction of GFP-myosin II at the cleavage furrow. Numbers at upper left of each frame are time in seconds. Time 0 is the first frame after photobleaching. The frame below is one  $\tau$  time unit (e-fold time) after photobleaching measured for the presented cell. Frequency histograms show the distributions of immobile fractions (means  $\pm$  SEM and sample sizes are listed). WT control and 14-3-3OE are indistinguishable. The myosin II immobile fraction for WT:14-3-3hp is significantly higher (ST:  $p < 0.001^*$ ) than that found in WT and WT:14-3-3OE cell lines.

(E) 14-3-3 protein shifts the myosin II bipolar thick filament assembly equilibrium in vitro. Purified myosin II shows ~20% soluble (unassembled) myosin II in the salt range of 25–100 mM NaCl. With the addition of equimolar 14-3-3 (250 nM dimer) at 25 and 50 mM NaCl, more myosin II remains soluble (ST:  $p < 0.05^*$ ). The mean  $\pm$  SEM ( $n = 6-7$ ) is provided for each salt concentration.

(F) Cartoon model showing the pathway elucidated in the text whereby 14-3-3 connects microtubules and Rac to myosin II to control cortical mechanics, cell shape, and cytokinesis.

prove to be generalizable to other systems, because mammalian myosin II appeared on the list of potential 14-3-3 $\sigma$  interactors in a proteomics study [16]. Furthermore, 14-3-3 may contribute to myosin II activation in many ways, because it

has also been implicated in regulating mammalian myosin light chain phosphatase [28].

14-3-3 also functions downstream of RacE: its cortical localization depends on RacE; its solubility depends on

RacE and GTP; and its overexpression in *RacE* null cells partially rescues the growth, cortical tension, and cytokinesis defects. Though we were unable at this time to demonstrate direct binding between 14-3-3 and RacE, these data demonstrate that 14-3-3 links at least indirectly to RacE. These data also suggest that the cortical localization of 14-3-3 reflects where active RacE is found. RacE is uniformly distributed around the plasma membrane during cell division [29] and may regulate one or more of the global/polar-module proteins [1]. Significantly, 14-3-3 enriches all along the cell cortex but is reduced in the cleavage furrow region. Because myosin II was still able to accumulate in the cleavage furrow cortex in the 14-3-3hp cells, active RacE may promote 14-3-3 accumulation in the polar cortex where it helps remodel the myosin II BTFs.

14-3-3 may also modify the function of several other cortical actin-associated proteins such as dynacortin, fimbrin, coronin, enlazin, and LimE [30]. Several of these proteins contain predicted consensus 14-3-3 binding motifs and are found in concentrations comparable to 14-3-3. Fimbrin appeared on the list of potential interactors (Figure S4B); however, we have been unable thus far to recapitulate the fimbrin-14-3-3 interaction via standard coimmunoprecipitation assays. This is possibly due to fimbrin's short cortical association time (260 ms) [3]. Interestingly, 14-3-3 proteins often bind to phosphorylated ligands, and a number of phosphorylated proteins reside in the cortex (e.g., dynacortin is a phosphoprotein [1]). Similarly, sea urchin embryos accumulate multiple cortical phosphoproteins during cell division, and this accumulation is inhibited by nocodazole treatment [31].

Finally, microtubules contribute to cortical mechanics, probably through a signaling pathway that includes 14-3-3. In return, 14-3-3 contributes to the steady-state microtubule structures and modulates cortical mechanics through RacE and myosin II (Figure 4F). Therefore, this is not a linear pathway but what appears to be a circular (feedback) system between the microtubules and the cortex. The combination of these observations then leads to the question of whether the manner in which the spindle regulates the cortex is really through a feedback system where the spindle directs the cortex and the cortex directs the spindle [32]. In this case, cytokinesis symmetry breaking may occur through bidirectional communication between these two structures. Similar ideas have been suggested elsewhere [33, 34]. Overall, 14-3-3 coordinates three major cytoskeletal elements—microtubules, actin, and myosin II—to control two critical processes, cytokinesis fidelity and cortical mechanics.

## Experimental Procedures

Experimental procedures for *Dictyostelium* strains, cell culture and plasmids, cDNA library screening, cell growth in suspension and growth rate determination, RNAi analysis, DAPI staining and nuclei/cell ratio determination, antibody production and western analysis, immunocytochemistry, cytokinesis analysis, microtubule analysis, actin wave analysis, effective cortical tension measurements, anti-FLAG coimmunoprecipitation, mass spectrometry analysis, 14-3-3-myosin II coimmunoprecipitation, FRAP analysis, and in vitro BTF assembly can be found in Supplemental Experimental Procedures. For statistical analysis, significance was determined by two-tailed Student's *t* test, Mann-Whitney nonparametric test, or comparing proportions (CP) where the standard error is defined as  $SE = \sqrt{(f(1-f)/n)}$ , where *f* is the fraction of cells showing a behavior and *n* is the sample size. The *p* values are provided for each test in the relevant figure legends; for CP, the *z* values are also provided.

## Supplemental Information

Supplemental Information includes Supplemental Experimental Procedures, four figures, and two tables and can be found with this article online at doi:10.1016/j.cub.2010.09.048.

## Acknowledgments

We thank the members of the Robinson laboratory for helpful comments on the manuscript and Cathy Kabacoff in particular for assistance with generating cell lines. This work was supported by an American Heart Fellowship (to Q.Z.), National Institutes of Health (NIH) grant GM066817 (to D.N.R.), American Cancer Society grant RSG CCG-114122 (to D.N.R.), National Science Foundation grant CCF 0621740 (to P.A.I. and D.N.R.), NIH grant GM86704 (to P.A.I. and D.N.R.), and NIH grant GM082834 (to U.S.E.).

Received: April 5, 2010

Revised: August 12, 2010

Accepted: September 15, 2010

Published online: October 14, 2010

## References

- Robinson, D.N., and Spudich, J.A. (2000). Dynacortin, a genetic link between equatorial contractility and global shape control discovered by library complementation of a *Dictyostelium discoideum* cytokinesis mutant. *J. Cell Biol.* 150, 823–838.
- Zhang, W., and Robinson, D.N. (2005). Balance of actively generated contractile and resistive forces controls cytokinesis dynamics. *Proc. Natl. Acad. Sci. USA* 102, 7186–7191.
- Reichl, E.M., Ren, Y., Morphew, M.K., Delannoy, M., Effler, J.C., Girard, K.D., Divi, S., Iglesias, P.A., Kuo, S.C., and Robinson, D.N. (2008). Interactions between myosin and actin crosslinkers control cytokinesis contractility dynamics and mechanics. *Curr. Biol.* 18, 471–480.
- Bringmann, H., and Hyman, A.A. (2005). A cytokinesis furrow is positioned by two consecutive signals. *Nature* 436, 731–734.
- Wheatley, S.P., and Wang, Y.-L. (1996). Midzone microtubule bundles are continuously required for cytokinesis in cultured epithelial cells. *J. Cell Biol.* 135, 981–989.
- Alsop, G.B., and Zhang, D. (2004). Microtubules continuously dictate distribution of actin filaments and positioning of cell cleavage in grasshopper spermatocytes. *J. Cell Sci.* 117, 1591–1602.
- Glotzer, M. (2005). The molecular requirements for cytokinesis. *Science* 307, 1735–1739.
- Eggert, U.S., Mitchison, T.J., and Field, C.M. (2006). Animal cytokinesis: From parts list to mechanisms. *Annu. Rev. Biochem.* 75, 543–566.
- Li, H., Chen, Q., Kaller, M., Nellen, W., Gräf, R., and De Lozanne, A. (2008). *Dictyostelium* Aurora kinase has properties of both Aurora A and Aurora B kinases. *Eukaryot. Cell* 7, 894–905.
- Chen, Q., Lakshmikanth, G.S., Spudich, J.A., and De Lozanne, A. (2007). The localization of inner centromeric protein (INCENP) at the cleavage furrow is dependent on Kif12 and involves interactions of the N terminus of INCENP with the actin cytoskeleton. *Mol. Biol. Cell* 18, 3366–3374.
- Kurz, T., Pintard, L., Willis, J.H., Hamill, D.R., Gönczy, P., Peter, M., and Bowerman, B. (2002). Cytoskeletal regulation by the Nedd8 ubiquitin-like protein modification pathway. *Science* 295, 1294–1298.
- Neujahr, R., Albrecht, R., Köhler, J., Matzner, M., Schwartz, J.-M., Westphal, M., and Gerisch, G. (1998). Microtubule-mediated centrosome motility and the positioning of cleavage furrows in multinucleate myosin II-null cells. *J. Cell Sci.* 111, 1227–1240.
- Bringmann, H., Cowan, C.R., Kong, J., and Hyman, A.A. (2007). LET-99, GOA-1/GPA-16, and GPR-1/2 are required for aster-positioned cytokinesis. *Curr. Biol.* 17, 185–191.
- Nagasaki, A., and Uyeda, T.Q. (2008). Chemotaxis-mediated scission contributes to efficient cytokinesis in *Dictyostelium*. *Cell Motil. Cytoskeleton* 65, 896–903.
- Saurin, A.T., Durgan, J., Cameron, A.J., Faisal, A., Marber, M.S., and Parker, P.J. (2008). The regulated assembly of a PKCepsilon complex controls the completion of cytokinesis. *Nat. Cell Biol.* 10, 891–901.
- Wilker, E.W., van Vugt, M.A., Artim, S.A., Huang, P.H., Petersen, C.P., Reinhardt, H.C., Feng, Y., Sharp, P.A., Sonenberg, N., White, F.M., and Yaffe, M.B. (2007). 14-3-3sigma controls mitotic translation to facilitate cytokinesis. *Nature* 446, 329–332.



17. Ottaviani, E., Effler, J.C., and Robinson, D.N. (2006). Enlazin, a natural fusion of two classes of canonical cytoskeletal proteins, contributes to cytokinesis dynamics. *Mol. Biol. Cell* 17, 5275–5286.
18. Robinson, D.N., Ocon, S.S., Rock, R.S., and Spudich, J.A. (2002). Dynactin is a novel actin bundling protein that localizes to dynamic actin structures. *J. Biol. Chem.* 277, 9088–9095.
19. Prassler, J., Stocker, S., Marriott, G., Heidecker, M., Kellermann, J., and Gerisch, G. (1997). Interaction of a Dictyostelium member of the plastin/fimbrin family with actin filaments and actin-myosin complexes. *Mol. Biol. Cell* 8, 83–95.
20. Robinson, D.N., Cavet, G., Warrick, H.M., and Spudich, J.A. (2002). Quantitation of the distribution and flux of myosin-II during cytokinesis. *BMC Cell Biol.* 3, 4.
21. Zhang, L., Wang, H., Liu, D., Liddington, R., and Fu, H. (1997). Raf-1 kinase and exoenzyme S interact with 14-3-3zeta through a common site involving lysine 49. *J. Biol. Chem.* 272, 13717–13724.
22. Gerald, N., Dai, J., Ting-Beall, H.P., and De Lozanne, A. (1998). A role for Dictyostelium racE in cortical tension and cleavage furrow progression. *J. Cell Biol.* 141, 483–492.
23. Bretschneider, T., Anderson, K., Ecke, M., Müller-Taubenberger, A., Schroth-Diez, B., Ishikawa-Ankerhold, H.C., and Gerisch, G. (2009). The three-dimensional dynamics of actin waves, a model of cytoskeletal self-organization. *Biophys. J.* 96, 2888–2900.
24. Lakshmikanth, G.S., Warrick, H.M., and Spudich, J.A. (2004). A mitotic kinesin-like protein required for normal karyokinesis, myosin localization to the furrow, and cytokinesis in Dictyostelium. *Proc. Natl. Acad. Sci. USA* 101, 16519–16524.
25. Egelhoff, T.T., Lee, R.J., and Spudich, J.A. (1993). Dictyostelium myosin heavy chain phosphorylation sites regulate myosin filament assembly and localization in vivo. *Cell* 75, 363–371.
26. Nock, S., Liang, W., Warrick, H.M., and Spudich, J.A. (2000). Mutational analysis of phosphorylation sites in the Dictyostelium myosin II tail: Disruption of myosin function by a single charge change. *FEBS Lett.* 466, 267–272.
27. Yumura, S., Yoshida, M., Betapudi, V., Licate, L.S., Iwamoto, Y., Nagasaki, A., Uyeda, T.Q., and Egelhoff, T.T. (2005). Multiple myosin II heavy chain kinases: Roles in filament assembly control and proper cytokinesis in Dictyostelium. *Mol. Biol. Cell* 16, 4256–4266.
28. Koga, Y., and Ikebe, M. (2008). A novel regulatory mechanism of myosin light chain phosphorylation via binding of 14-3-3 to myosin phosphatase. *Mol. Biol. Cell* 19, 1062–1071.
29. Larochelle, D.A., Vithalani, K.K., and De Lozanne, A. (1997). Role of Dictyostelium racE in cytokinesis: Mutational analysis and localization studies by use of green fluorescent protein. *Mol. Biol. Cell* 8, 935–944.
30. Schneider, N., Weber, I., Faix, J., Prassler, J., Müller-Taubenberger, A., Köhler, J., Burghardt, E., Gerisch, G., and Marriott, G. (2003). A Lim protein involved in the progression of cytokinesis and regulation of the mitotic spindle. *Cell Motil. Cytoskeleton* 56, 130–139.
31. Walker, G.R., Shuster, C.B., and Burgess, D.R. (1997). Microtubule-entrained kinase activities associated with the cortical cytoskeleton during cytokinesis. *J. Cell Sci.* 110, 1373–1386.
32. Robinson, D.N., Kee, Y.-S., Luo, T., and Surcel, A. (2010). Biophysics of cell division: Understanding how dividing cells change shape. In *Comprehensive Biophysics, Volume 7*, D. Wirtz and E.H. Egelman, eds. (Amsterdam: Elsevier), in press.
33. Hu, C.K., Coughlin, M., Field, C.M., and Mitchison, T.J. (2008). Cell polarization during monopolar cytokinesis. *J. Cell Biol.* 181, 195–202.
34. Giansanti, M.G., Bonaccorsi, S., Williams, B., Williams, E.V., Santolamazza, C., Goldberg, M.L., and Gatti, M. (1998). Cooperative interactions between the central spindle and the contractile ring during Drosophila cytokinesis. *Genes Dev.* 12, 396–410.

## Supplemental Information

### 14-3-3 Coordinates Microtubules,

### Rac, and Myosin II to Control

### Cell Mechanics and Cytokinesis

Qiongqiong Zhou, Yee-Seir Kee, Christopher C. Poirier, Christine Jelinek, Jonathan Osborne, Srikanth Divi, Alexandra Surcel, Marie E. Will, Ulrike S. Eggert, Annette Müller-Taubenberger, Pablo A. Iglesias, Robert J. Cotter, and Douglas N. Robinson

#### Supplemental Experimental Procedures

##### ***Dictyostelium* Strains, Cell Culture, and Plasmids**

*Dictyostelium discoideum* strains include wild type Ax3 (Rep orf+ cells), *cortI*<sup>1151</sup>,  $\Delta$ *RacE*, *RacE*<sup>24E</sup> (REMI insertional mutant), and myosin II heavy chain null mutant (*mhcA* (HS1)) [1-3] (Table SI). *RacE*: 14-3-3 suppression experiments were performed in both *RacE* mutant backgrounds with similar results. Cells were grown in Hans' enriched HL-5 media (1.4xHL-5 plus 8% FM) plus 60 U/ml penicillin, 60  $\mu$ g/ml streptomycin sulfate and plus or minus selecting drugs, depending on whether the cells were transformed with an episomal plasmid (Table SI). Electroporation was performed to transform plasmids into *Dictyostelium* cells using a Genepulser-II electroporator. Cells transformed with pLD1A15SN-based plasmids were selected with 10-15  $\mu$ g/ml of G-418, and cells transformed with pDRH plasmid were selected with 30  $\mu$ g/ml of hygromycin. Cells were propagated at 22°C on 10-cm plates. For suspension culture, cells were grown in 10-ml culture volumes in 125-ml Erlenmeyer flasks at 200 rpm. Cell densities were measured using a hemacytometer.

LimE $\Delta$ coil-GFP was constructed in pDRH according to Schneider *et al.*, 2003 [4]. 14-3-3-GFP was constructed from an in-house GFP-tagging cassette and cloned into pLD1A15SN [3]. 14-3-3(K49E)-GFP was constructed using QuickChange II Site-Directed Mutagenesis Kit (Agilent Technologies) and the pLD1A15SN: 14-3-3-GFP as the host plasmid. The complete 14-3-3(K49E)-GFP cDNA sequence was confirmed by sequencing. GFP-RacE and GFP-tubulin plasmids were described previously [3, 5]. The mCherry-RacE expression plasmid was constructed by first generating an mCherry-tagging cassette in pBlueScript, similar to our GFP-tagging system described previously [3, 5], and then sub-cloning the mCherry-RacE into pDRHyg [5]. The pLD1A15SN: Enl-tr plasmid was described previously [6].

##### **cDNA Library Screening**

A *Discoideum discoideum* cDNA library prepared from vegetative cells was transformed into Ax3(Rep orf+) cells as described previously [3]. 100 pools of transformants (1000 transformants/pool) were cultured in suspension with nocodazole at the IC<sub>50</sub> concentration for approximately two weeks. Cells were split and fresh media with drug was added either when the density reached 2 x 10<sup>6</sup> cells/ml or every four days. Cells were collected and plasmid DNA was isolated using a Wizard Plus Miniprep kit (Promega, Madison, WI). The isolated plasmid DNA was then transformed into STBL2 (Invitrogen, Carlsbad, CA) cells. Once isolated, plasmid DNA was sequenced and identified using Dictybase BLAST. The plasmid was reintroduced into

Ax3(Rep orf+) cells to confirm that the rescued growth rate in nocodazole was due to the isolated plasmid.

### **Cell Growth in Suspension and Growth Rate Determination**

Cells grown on plates were resuspended and grown in suspension culture at an initial concentration of  $\sim 2 \times 10^5$  cells/ml. Cell concentrations were determined daily using a hemacytometer. The cell densities were plotted versus time and the resulting log phase curve was fit to a single exponential equation. The wild-type control strain was normalized to 1, and growth rates of other strains within each growth experiment were normalized to the wild-type control. The relative growth rates for each strain were averaged, and the standard error of the mean (SEM) was determined.

### **RNAi Analysis**

The 14-3-3 hairpin construct (14-3-3hp) was generated by cloning bases 16-343 in the antisense orientation in the *Sal* I and *Not* I sites of pLD1A15SN, generating the construct pLD1A15SN:14-3-3AS. The sense fragment spanning bases 261-343 was ligated into the *Not* I and *Mlu* I sites of pLD1A15SN:14-3-3AS, generating pLD1A15SN:14-3-3hp. Sequences that contributed to the stem region of the RNAi hairpin were blasted against Dictybase (<http://dictybase.org>), and it was determined that there are no stretches with  $\geq 16$  out of 20 base pair identities to genes other than 14-3-3, thus eliminating the possibility of nonspecific RNAi. To achieve partial knockdown of 14-3-3, we initially selected the transformed cells with 15  $\mu$ g/ml G418 for two days, then shifted the drug to 7.5  $\mu$ g/ml G418 from then on. This method consistently reduced 14-3-3 expression by 70% across many independent transformations. 14-3-3 mRNA and protein levels were determined by real-time RT-PCR (Bio-Rad, Hercules, CA), and Western analysis, respectively. The protein concentrations were determined by Bradford (Bio-Rad, Hercules, CA), and dynacortin levels were assessed to confirm equal loading.

### **DAPI Staining and Nuclei/Cell Ratio Determination**

Cells were plated on coverslips and allowed to adhere for 20 min. Cells were then fixed with cold methanol and stained with 1  $\mu$ g/ml DAPI in phosphate buffered saline (1xPBS), 90% glycerol. Cells were examined by fluorescence microscopy using a motorized Olympus IX81 microscope (Olympus American, Melville, NY).

### **Antibody Production and Western Analysis**

The full length 14-3-3 was expressed in *Escherichia coli* as a His-tagged protein using the pET22b vector (Novagen, Madison, WI). 14-3-3-His protein was purified on a  $\text{Ni}^{2+}$  Super-flow resin (GE Healthcare, WI), followed by an UnoQ column (Bio-Rad, Hercules, CA). Rabbit polyclonal antibodies were generated using a standard protocol for antibody production (Josman, LLC<sup>TM</sup>, Napa, CA). For Western analysis, cell lysates were prepared by boiling cells in SDS sample buffer, electrophoretically separated on SDS-polyacrylamide gels, and transferred to nitrocellulose. 14-3-3 protein was detected using the anti-14-3-3 polyclonal antibody and a goat anti-rabbit, horseradish peroxidase-conjugated, secondary antibody (Bio-Rad, Hercules, CA). Immune complexes were detected using the ECL detection system (Thermo Fisher Scientific, Rockford, IL) and a Versa Doc imaging station (Bio-Rad, Hercules, CA).

### **Immunocytochemistry**

Cells were plated on cover-slips overnight, then cells were fixed for 15 min in fixation buffer (4% paraformaldehyde, 150 mM NaCl, 0.1% Triton X-100). After washing with 1xPBS, cells were blocked with 1% BSA in 1xPBS, followed by incubation with the anti-14-3-3 polyclonal antibodies (1:750) in 1xPBS. Antibodies were detected by indirect immunofluorescence using

TRITC-conjugated chicken anti-rabbit secondary antibodies (1:500) (Santa Cruz Biotechnology, Santa Cruz, CA) or FITC-conjugated goat anti-rabbit secondary antibodies (1:750) (Sigma-Aldrich, St. Louis, MO).

### **Cytokinesis Analysis**

Cells were cultured in a Lab-Tek™ 8-well-chamber (Thermo Fisher Scientific, Rochester, NY) overnight before imaging. Differential interference contrast (DIC) movies of dividing cells were collected with 2-s time resolution, and furrow ingression dynamics were analyzed as described previously [7]. Briefly, the minimal furrow diameter and furrow length at 4-s time resolution were measured in Image-J (<http://rsbweb.nih.gov/ij/>). The time point when the length and diameter were equal (the crossover distance,  $D_x$ ) was defined as time=0 s. The rescaled diameter then is the actual diameter normalized by  $D_x$ . Daughter cell symmetry was assessed by measuring the two dimensional area of freshly generated daughter cells using Image-J. The ratio of areas of the two daughter cells (normalizing with respect to the smaller cell) was calculated.

### **Analysis of Interphase and Spindle Microtubule Dimensions and Dynamics**

Cells expressing GFP-tubulin were transferred to an imaging chamber and allowed to attach. Then, cells were incubated either with 0.1% DMSO (the solvent for nocodazole) or 10- $\mu$ M nocodazole for 30 min. For total microtubule length measurements, cells were flattened with a sheet of agarose followed by immediate fluorescence imaging. The total microtubule length is the average length of the microtubules from the centrosome to the tip. Movies of microtubule movements were collected with 1-s time resolution using a 60x objective and a 1.6x optovar. The microtubule lengths were measured using Image-J by tracking microtubules by following their side-to-side fluctuations. Interphase microtubules in *Dictyostelium* are thought to have minimal dynamic instability so that individual microtubule growth and catastrophe dynamics are nominal for this analysis.

For the microtubule contact length and cortical association times, TIRF movies of microtubule movements were collected with 0.33-s time resolution using a 60x objective and a 1.6x optovar. The microtubule contact lengths and cortical association times were measured using in-house software developed in MatLab (Mathworks, Natick, MA). A semi-automated tracking analysis was conducted to follow the microtubule location and duration of cortex association. A microtubule association event was characterized as the total length of consecutive frames a microtubule was present in the TIRF plane without interruption. For each microtubule association event, the maximum length, average length and association time were recorded. The association times and the measured lengths were binned and converted into probability distributions.

To assess the dynamics of the mitotic spindle, we developed a custom MatLab (Mathworks, Natick, MA) graphical user interface (GUI). Time-lapse movies of cells expressing GFP-tubulin were loaded into the GUI and the spindle end points were extracted at each time-point. Spindle length and angle were measured for each time-point. To align the data, spindle length was normalized to the maximum spindle length achieved, and the spindle lengths were aligned so that their y-intercept was 0.5 at time=0 s. Using the measurement interval and the image resolution, the velocity and angular speed were computed. The angular velocity was computed by taking the difference of adjacent spindle angle measurements and dividing by the elapsed time. The angular speed is the absolute value of the angular velocity. The aligned spindle length and angular velocity plots were averaged over time, and a standard error was computed based on the standard deviation and the number of data points at each time point.

### **Actin Wave Analysis**

Wild type cells were cotransformed with GFP-limE $\Delta$ coil plasmid and the empty vector, 14-3-3hp, or 14-3-3-OE plasmid. Expression levels of 14-3-3 were verified by Western analysis to ensure



a 70% down regulation in hairpin transformed cells. Cells were then cultured in HL-5 media in a Lab-Tek™ 8-well-chamber and GFP-TIRF movies were collected with 1-s intervals and 100-ms exposure time. Actin waves were detected and counted manually in Image-J by the indication of GFP-limEΔcoil. Wave velocity was calculated manually by measuring wave travel distance and time interval. Wave amplitude and wave width (time duration) were calculated using an automated algorithm written as a Java plug-in in ImageJ 1.40g. The algorithm implemented a peak detection method to identify wave maxima. Wave amplitude was normalized by dividing the maximum value by the cytoplasmic background fluorescence. Wave width was measured as the difference in time from the rise of the peak to the fall of the peak.

### Cortical Tension Measurements

The cortical tension of interphase cells was measured using micropipette aspiration as described previously [8]. In short, micropipettes were pulled to an inner diameter of 6 μm (PMP102 micropipette puller; MicroData Instruments, Woodhaven, NY) and filled with sterile MES starvation buffer (50 mM MES, pH 6.8, 2 mM MgCl<sub>2</sub>, 0.2 mM CaCl<sub>2</sub>). Log-phase cells were transferred to imaging chambers and allowed to settle for 15 min. Cells were aspirated until the equilibrium length of the cortex tether pulled into the pipette ( $L_p$ ) was equal to the radius of the pipette ( $R_p$ ), forming a hemispherical deformation ( $L_p/R_p = 1$ ). The effective cortical tension ( $T_{eff}$ ) [6, 9] was calculated using the Young-Laplace equation:  $\Delta P = 2T_{eff}(1/R_p - 1/R_c)$  where  $\Delta P$  is the applied pressure that produced the hemispherical deformation and  $R_c$  is the radius of the cell.

### Anti-FLAG Coimmunoprecipitation and Mass Spectrometry Analysis

Logarithmically growing WT control and WT:14-3-3-FLAG cells were collected, washed with 1xPBS, and lysed in lysis buffer (20 mM Tris, 100 mM NaCl, 1 mM EDTA and 0.1% NP-40, pH 7.4) at a cell density of  $1 \times 10^7$  cells/ml. After incubating on ice for 30 min (vortexing once every 10 min), the lysates were centrifuged at 10,000xg for 10 min. Protein concentration was determined using a Bradford assay. After preclearing with agarose-bead-conjugated mouse IgG (Sigma-Aldrich, St. Louis, MO) for 30 min, the lysate was incubated with agarose-bead-conjugated-anti-FLAG antibody (Sigma-Aldrich, St. Louis, MO) for 1 hr then washed 3 times in 1xTBS. Bound proteins were eluted with 3xFLAG peptide (Sigma-Aldrich, St. Louis, MO) for SDS-PAGE gels or with non-reducing sample buffer for mass spectrometry analysis. Following protein separation via SDS-PAGE, protein was stained with SyproRuby (Sigma-Aldrich, St. Louis, MO), subsequent protein bands were excised from the gel material, cut into 1-mm pieces, and digested in-gel overnight at 37°C with 0.4 μg of trypsin prepared in 1 mM HCl, using the protocol and reagents provided in the Trypsin Profiler IGD Kit for in-gel digestions (Sigma-Aldrich, St. Louis, MO) [10]. Proteins eluted with non-reducing sample buffer were subjected to an in-solution tryptic digestion. These aliquots were resuspended in 50 mM ammonium bicarbonate and incubated with a 1:20 ratio of trypsin enzyme at 37°C overnight. Resultant peptides from both in-gel digestion and in-solution digestion were isolated and lyophilized to dryness before mass spectrometric analysis. Once pelleted, samples were reconstituted in 10 μL of water with 0.1% fluoroacetic acid (FA) (Pierce, Rockford, IL).

Ten-μL aliquots of each resuspended tryptic protein digest were placed in the Agilent 1200 autosampler (Agilent, Santa Clara, CA). Eight microliters of each 10-μL sample were loaded by the autosampler onto a fused silica PicoFrit (New Objective, Woburn, MA) capillary column, 75-μm inner diameter (i.d.) x120 mm long column packed in-house with 5 μm, 300 Å BioBasic C<sub>18</sub> (Thermo Electron, Bremen, Germany) stationary phase. Peptides were separated on-line via reversed phase nano high-performance liquid chromatography using the Eksigent Nano 2D high-performance liquid chromatography (HPLC) pumping system (Eksigent, Dublin, CA). The Eksigent Nano 2D HPLC system was controlled by XCalibur software, Version 2.0 (Thermo Electron, San Jose, CA). Separations were performed at a mobile phase flow rate of 300 nL/min on the binary pump system using a 10-90% linear gradient of mobile phase A (0.1 %

formic acid in deionized water) and mobile phase B (90% (vol/vol) acetonitrile with 0.1% (vol/vol) formic acid). Run times were 60 min for each sample prepared during the in-gel digest and 200 min for each sample prepared during the in-solution digest. The outlet flow of the nano-HPLC interfaced directly with the inlet of an LTQ-Orbitrap-XL (Thermo Electron, San Jose, CA), allowing for introduction of the analyte into the mass spectrometer.

**Tandem Mass Spectrometric Analysis (LTQ-Orbitrap XL).** The LTQ-OrbitrapXL mass spectrometer was operated in *data dependent* mode. MS precursor scan spectra ( $m/z$  300-2000) were acquired in the Orbitrap with mass resolution of one part in 60,000; the five most intense ions from each MS scan were automatically targeted for fragmentation (MS/MS) in the ion trap. Using helium as the collision gas, collision-induced dissociation (CID) mediated peptide fragmentation in the linear ion trap. The LTQ-OrbitrapXL was controlled by XCalibur software. For each experiment, the source voltage was set at 2.2 V, capillary voltage at 48 V, and the capillary temperature was set at 200°C. Sheath and auxiliary gases were not necessary because nanoflow parameters were being used. The tube lens voltage was kept at 105 V, and the ion-gate pressure was  $1.5 \times 10^{-5}$  Torr. The ion trap AGC was set at 30,000. Normalized collision energy was established at 35% for MS/MS. The default charge state was set at two. The isolation window for the ion gate was fixed at two Daltons. After an initial MS/MS fragmentation event, ions were excluded from additional fragmentation rounds for 30 sec using dynamic exclusion. The ion selection threshold, the minimum signal required to trigger tandem mass spectrometry, was set to 500. The activation Q was set at 0.25.

**Peptide Identification via MASCOT Database Search.** Peptides were identified and confirmed via automated database searching using the MASCOT search algorithm (Matrix Science, Boston, MA). Our experimental data was searched against the RefSeq 35 FASTA database with a mass tolerance of 10 ppm established for MS species and 1 Da for MS/MS. Trypsin was selected as the proteolytic enzyme. Up to two missed cleavage events were allowed. Automatic charge state assignment was applied for all MS data. Search results were combined and then filtered using standard reporting criteria [11]. All peptide species meeting the minimum MASCOT score and validation requirements were then imported into ProteinCenter (Proxeon, Odense, Denmark) and Scaffold (Proteome Software, Portland, Oregon) for subsequent data mining.

**Peptide Quantification.** To determine which of the 274 proteins identified in the MASCOT to Scaffold proteomics platform were up- or down-regulated in either the experimental group or the control group, a spectral counting-based quantification strategy was used. To determine which peptides were significantly differentially expressed in either of our two lysate conditions, we applied the G-test of independence method first proposed by Sokal and Rolf [12]. Here, we defined  $f_1$  as the normalized spectral counts/protein in the control sample (empty vector control immunoprecipitate sample), and  $f_2$  as the normalized spectral counts/protein in the experimental sample (the 14-3-3-FLAG immunoprecipitate sample). The equation used to determine the G value is given as  $G = 2f_1 \ln(f_1/(\text{avg}f_1)) + 2f_2 \ln(f_2/(\text{avg}f_2))$  whereby  $\text{avg}f_1 = \text{avg}f_2 = (f_1 + f_2)/2$ . Assuming a Chi-square distribution with one degree of freedom and a significant  $p$  value of  $<0.05$ , a protein was considered to be differentially expressed if its calculated G value was  $>3.841$ . Those proteins found in the 14-3-3-FLAG sample that meet this criterion are shown in Figure S4B. The normalized spectral count numbers used during our G-test analysis were determined within the Scaffold proteomics platform.

### 14-3-3-Myosin II Coimmunoprecipitation

Logarithmically growing wild type and *myoII*: GFP-3xAsp cells were collected and washed one time with 1xPBS. Cells were incubated in 1xPBS with 1 mM of ATP and 1 mM of  $\text{MgCl}_2$  for 5 min at room temperature. Then,  $1.8 \times 10^8$  cells were collected and lysed in 600  $\mu\text{l}$  lysis buffer (50 mM Tris pH 6.8, 150 mM NaCl, 0.1% NP-40, 1 mM ATP, 1 mM  $\text{MgCl}_2$ , 1x protease inhibitor cocktail, 1x phosphatase inhibitor cocktail I and 1x phosphatase inhibitor cocktail II). Cells were

kept on ice for 30 min with brief vortexing every 5 min. The lysate was cleared by centrifugation (16,000xg), and 300  $\mu$ l of supernatant was collected and incubated with 6  $\mu$ l of anti-myosin antibody or preimmune serum as control at 4°C for 1.5 hr. 50  $\mu$ l of protein A-agarose beads were then added into each vial and incubated at room temperature for 1.5 hr. Finally, the beads were washed three times with 1 ml of cold TBS and proteins were eluted in 20  $\mu$ l of 4x sample buffer by heating at 95°C for 10 min.

For the reciprocal colP using anti-14-3-3 polyclonal sera, logarithmically growing WT cells were collected and washed one time with 1xPBS.  $6 \times 10^7$  cells were then incubated in 20 ml of 1xPBS with 1 mM DSP at room temperature for 30 min. The crosslinking reagent was added to prevent the polyclonal sera from competing off myosin II. The crosslinking reaction was stopped by adding 20 mM of Tris and incubated for 15 min at room temperature. Cells were collected and lysed in 600  $\mu$ l lysis buffer and handled as above except that anti-14-3-3 antibody or preimmune serum were used in the immunoprecipitation. Finally, coimmunoprecipitates were eluted in 20  $\mu$ l of 4x sample buffer with 20%  $\beta$ -mercaptoethanol and heated at 95°C for 10 min.

### Fluorescence Recovery after Photobleaching (FRAP) Analysis

FRAP analysis was performed as described previously [8]. In short, after background subtraction and correction for photobleaching, the recovery times were measured by fitting to:

$$F(t) = f - ge^{-(1/\tau)t}$$

and the immobile fractions were calculated according to the following:

$$F_i = (1 - f)/(1 - f + g).$$

In these equations, f is the total fluorescence intensity after recovery and g is the intensity difference between f and the level remaining immediately after photobleaching.

### Bipolar Thick Filament Assembly

mCherry-myosin II or endogenous myosin II was purified from *myoII::mCherry*-myosin II pDRH or Ax3 cells, respectively [2], and BTF assembly assays were performed as described previously [13, 14]. Specifically, purified myosin II was resuspended in 4 mM HEPES (pH 7.4), 1 mM EDTA. 15  $\mu$ L of sample was mixed with 5  $\mu$ L 4xsalt (NaCl) to attain the final concentrations of 0, 25, 50, 75, 100, and 150 mM. Final protein concentrations were 250 nM “hexameric” monomer (where a monomer equals two heavy chains and four light chains) and 250 nM 14-3-3-His. After incubating on ice for 20 min., the assembled myosin II BTFs were separated from unassembled myosin II by centrifugation at 186,000xg for 15 min. Supernatant and pellet fractions were run on polyacrylamide gels, Coomassie-stained, and imaged on a BioRad VersaDoc. Protein amounts were quantified by densitometry.

## Supplemental References

1. Larochelle, D.A., Vithalani, K.K., and DeLozanne, A. (1996). A novel member of the *rho* family of small GTP-binding proteins is specifically required for cytokinesis. *J. Cell Biol.* 133, 1321-1329.
2. Ruppel, K.M., Uyeda, T.Q.P., and Spudich, J.A. (1994). Role of highly conserved lysine 130 of myosin motor domain. In vivo and in vitro characterization of site specifically mutated myosin. *J. Biol. Chem.* 269, 18773-18780.
3. Robinson, D.N., and Spudich, J.A. (2000). Dynacortin, a genetic link between equatorial contractility and global shape control discovered by library complementation of a *Dictyostelium* discoideum cytokinesis mutant. *J. Cell Biol.* 150, 823-838.
4. Schneider, N., Weber, I., Faix, J., Prassler, J., Müller-Taubenberger, A., Köhler, J., Burghardt, E., Gerisch, G., and Marriott, G. (2003). A Lim protein involved in the progression of cytokinesis and regulation of the mitotic spindle. *Cell Motil. Cytoskeleton* 56, 130-139.
5. Effler, J.C., Kee, Y.-S., Berk, J.M., Tran, M.N., Iglesias, P.A., and Robinson, D.N. (2006). Mitosis-specific mechanosensing and contractile protein redistribution control cell shape. *Curr. Biol.* 16, 1962-1967.
6. Ottaviani, E., Effler, J.C., and Robinson, D.N. (2006). Enlazin, a natural fusion of two classes of canonical cytoskeletal proteins, contributes to cytokinesis dynamics. *Mol. Biol. Cell* 17, 5275-5286.
7. Zhang, W., and Robinson, D.N. (2005). Balance of actively generated contractile and resistive forces controls cytokinesis dynamics. *Proc. Natl. Acad. Sci. USA* 102, 7186-7191.
8. Reichl, E.M., Ren, Y., Morpew, M.K., Delannoy, M., Effler, J.C., Girard, K.D., Divi, S., Iglesias, P.A., Kuo, S.C., and Robinson, D.N. (2008). Interactions between myosin and actin crosslinkers control cytokinesis contractility dynamics and mechanics. *Curr. Biol.* 18, 471-480.
9. Derganc, J., Božic, B., Svetina, S., and Žekš, B. (2000). Stability analysis of micropipette aspiration of neutrophils. *Biophys. J.* 79, 153-162.
10. Jiménez, C.R., Huang, L., Qiu, Y., and Burlingame, A. (2001). In-Gel Digestion of Proteins for MALDI-MS Fingerprint Mapping. *Curr. Protoc. Protein Sci.* Chapter 16.
11. Eng, J.K., McCormack, A.L., and Yates III, J.R. (1994). An approach to correlate tandem mass spectral data of peptides with amino acid sequences in a protein database. *J. Am. Soc. Mass Spectrom.* 5, 976-989.
12. Sokal, R.R., and Rohlf, F.J. (1994). *Biometry: the principles and practice of statistics in biological research.*, 3rd ed., (New York: Freeman).
13. Kubalek, E.W., Uyeda, T.Q., and Spudich, J.A. (1992). A *Dictyostelium* myosin II lacking a proximal 58-kDa portion of the tail is functional in vitro and in vivo. *Mol. Biol. Cell* 3, 1455-1462.
14. Egelhoff, T.T., Lee, R.J., and Spudich, J.A. (1993). *Dictyostelium* myosin heavy chain phosphorylation sites regulate myosin filament assembly and localization *in vivo*. *Cell* 75, 363-371.



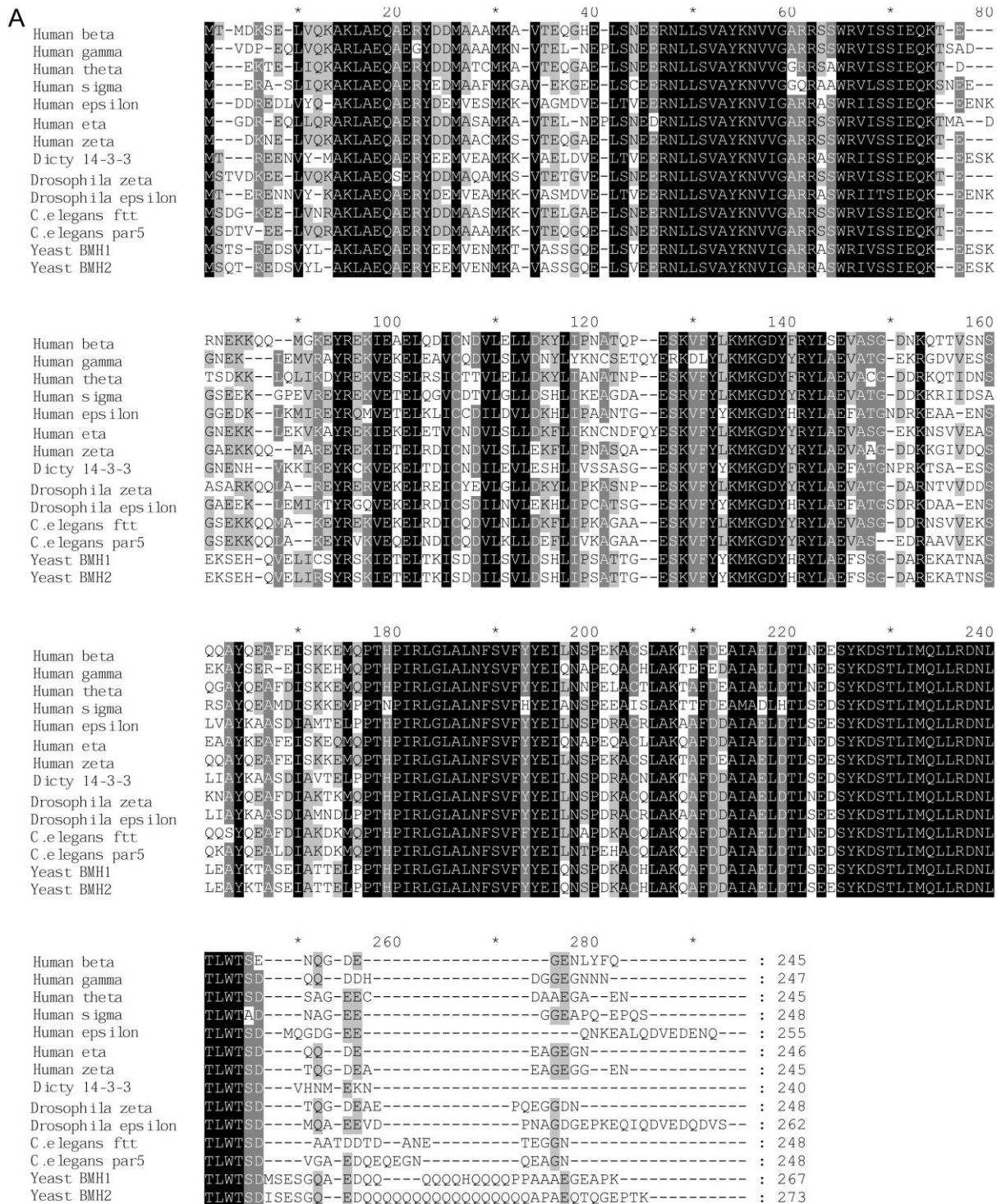


**Figure S1A.**

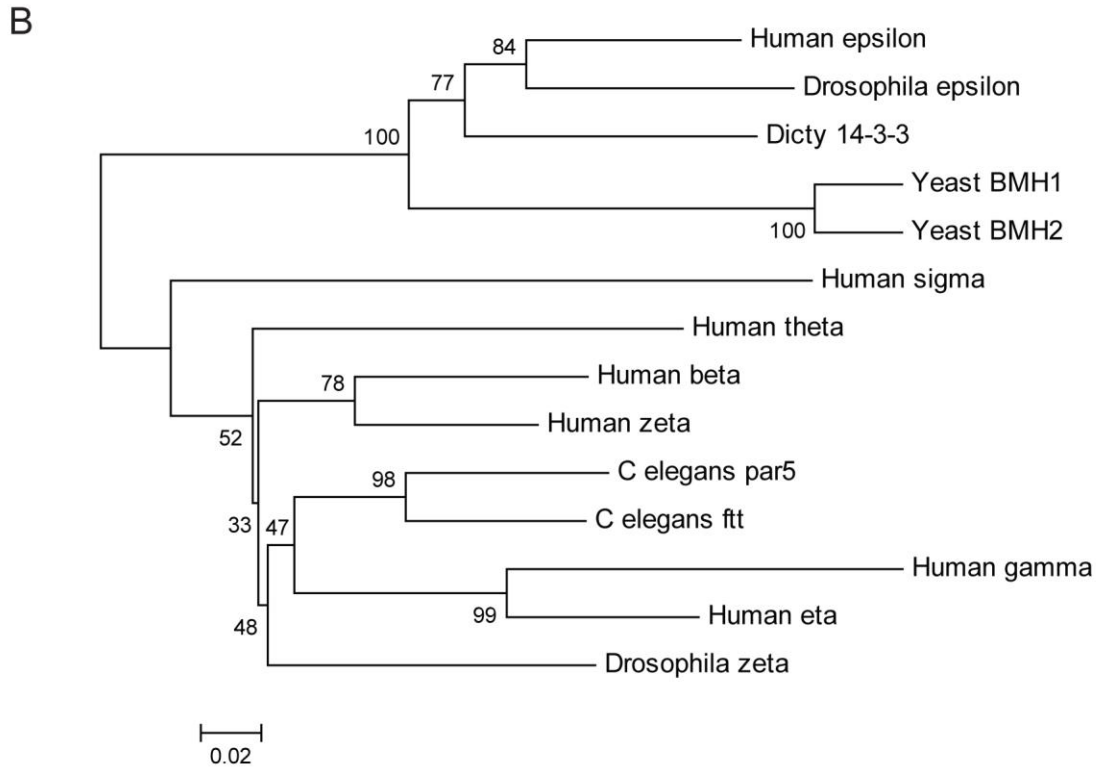


**Figure S1B.**

**Figure S1. Sequence Alignment and Phylogenetic Analysis of the 14-3-3 Family**

(A) Peptide sequence alignment of *Dictyostelium discoideum* 14-3-3 (Dicty 14-3-3), with seven human isoforms (Human beta, epsilon, eta, gamma, sigma, theta, and zeta), two *Drosophila melanogaster* isoforms (Drosophila epsilon, zeta), two *Caenorhabditis elegans* (C.elegans ftt and par5), and two *Saccharomyces cerevisiae* (Yeast BMH1 and BMH2). Sequences were obtained through ClustalW by blasting with *Dictyostelium* (Dicty) 14-3-3. The sequences were aligned using Clustal 2.0.11, following pairwise alignment parameters of 5 for gap opening, 0.5 for gap extension and BLOSUM30 for protein weight matrix and then manually adjusted using GeneDoc 2.6.

(B) Neighbor-joining tree showing the phylogenetic relationship of the 14-3-3 family with bootstrap values at each node. The tree was generated using MEGA 4.01.

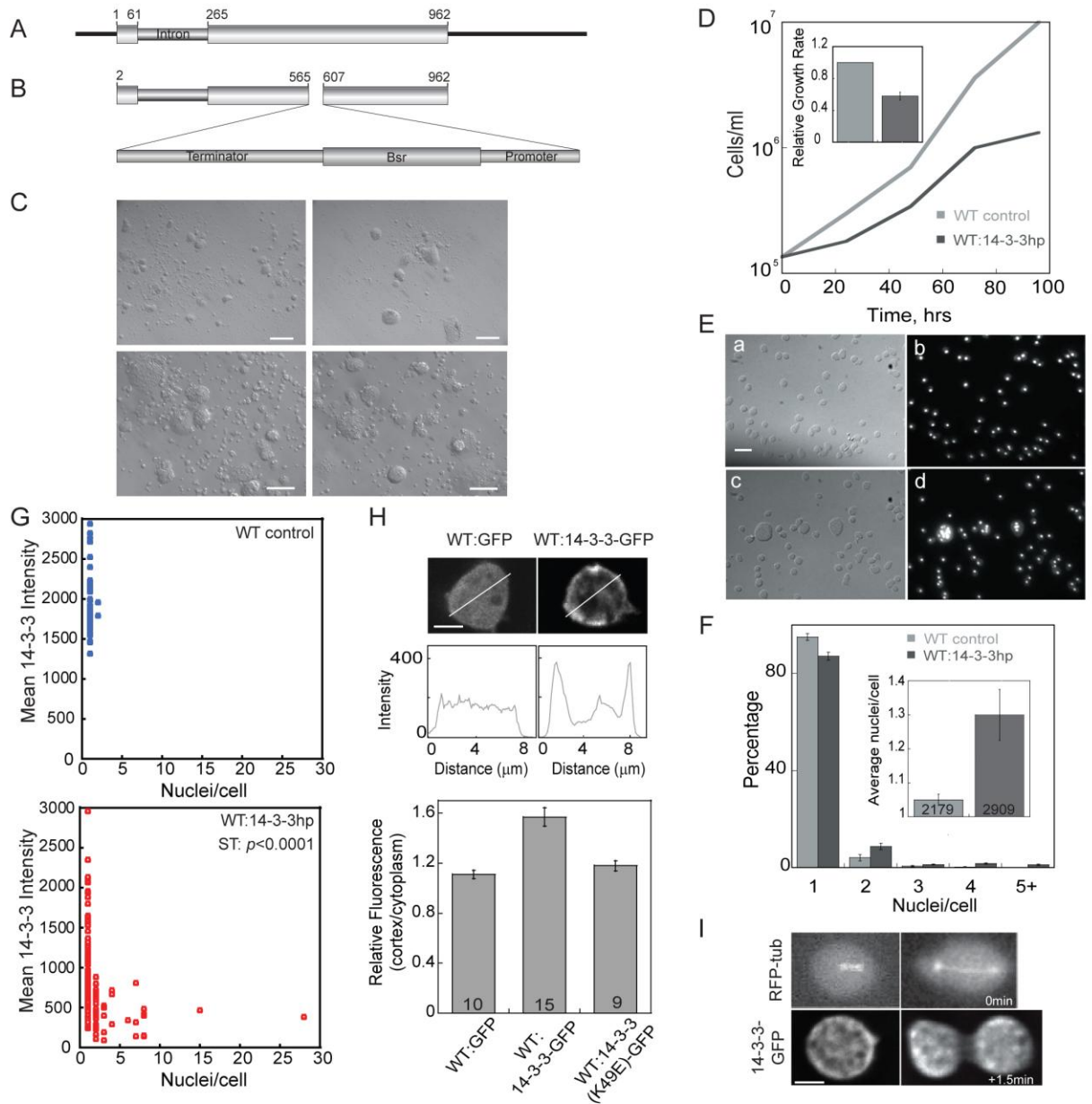


**Figure S2. 14-3-3 Is Required for Cytokinesis and Localizes to the Cortex**

(A) Schematic diagram of the *Dictyostelium* 14-3-3 (*fttB*) gene (DDB\_G0269138). Numbers indicate nucleotide positions of the exon borders.

(B) Diagram of the *fttB* gene disruption construct. The blasticidin resistance cassette (*bsr*) is flanked by two homologous fragments of the *fttB* gene as indicated.

(C) Micrographs of blasticidin-resistant clones that were observed after transformation of *Dictyostelium* cells with the construct shown in B. Bar in the upper figures corresponds to 250  $\mu$ m, in the lower figures to 100  $\mu$ m. These cells ultimately died, consistent with *fttB* being an essential gene.

(D) Representative growth curve for wild type and WT:14-3-3hp cells. Inset panel shows the relative growth rates of WT control cells (1.0) and WT:14-3-3hp cells (0.58),  $n=3$ . Error bars represent standard error of the mean.

(E) DAPI staining reveals multinucleated cells in WT:14-3-3hp cells. (Ea), DIC image of WT controls, (Eb), DAPI staining of WT controls, (Ec), DIC image of WT:14-3-3hp cells, (Ed), DAPI staining of WT:14-3-3hp cells. Scale bar, 40  $\mu\text{m}$ .

(F) Distribution of nuclei/cell from WT control cells and WT:14-3-3hp cells. Inset panel shows the average nuclei/cell of WT control cells and WT:14-3-3hp cells (ST:  $p=0.03$ ,  $n=6$  experiments. Total numbers of cells are shown on the bars). Error bars represent standard error of the mean.

(G) 14-3-3 levels correspond to the severity of the phenotype. The scatter plots show the average 14-3-3 intensity determined from immunocytochemistry plotted as a function of the number of nuclei for control and WT:14-3-3hp cells. Overall, 14-3-3hp cells had much lower overall 14-3-3 expression than control, and 14-3-3hp cells with 2 or more nuclei had significantly less 14-3-3 expression than mononucleated cells. Both comparisons are significant (ST:  $p<0.0001$ ).

(H) 3D-deconvolution of WT:GFP vs. WT:14-3-3-GFP demonstrates that 14-3-3 is enriched in the cell cortex. Line scan shows a flat signal across the WT: GFP cells and signal intensity peaks in the cortex of WT:14-3-3-GFP cells. The histogram shows the relative fluorescence intensity ratios (cortex/cytoplasm) of GFP signals from live-cell imaging of these strains and WT:14-3-3(K49E)-GFP cells (number of cells for each strain are shown on bars). Wild type 14-3-3-GFP had a significantly higher cortex to cytoplasm ratio (ST:  $p<0.0001$ ). Though not statistically significant overall, some cells expressing 14-3-3(K49E)-GFP showed some cortical enrichment. Error bars represent standard error of the mean.

(I) Live cell imaging of WT:14-3-3-GFP cells undergoing cytokinesis. Top panels show RFP-tubulin signal, confirming that cells are undergoing cell division. Bottom panel shows that 14-3-3-GFP is enriched in the cortex in early mitosis (left image) and in the global/polar cortex during cytokinesis (right image). Scale bar, 5  $\mu\text{m}$ .



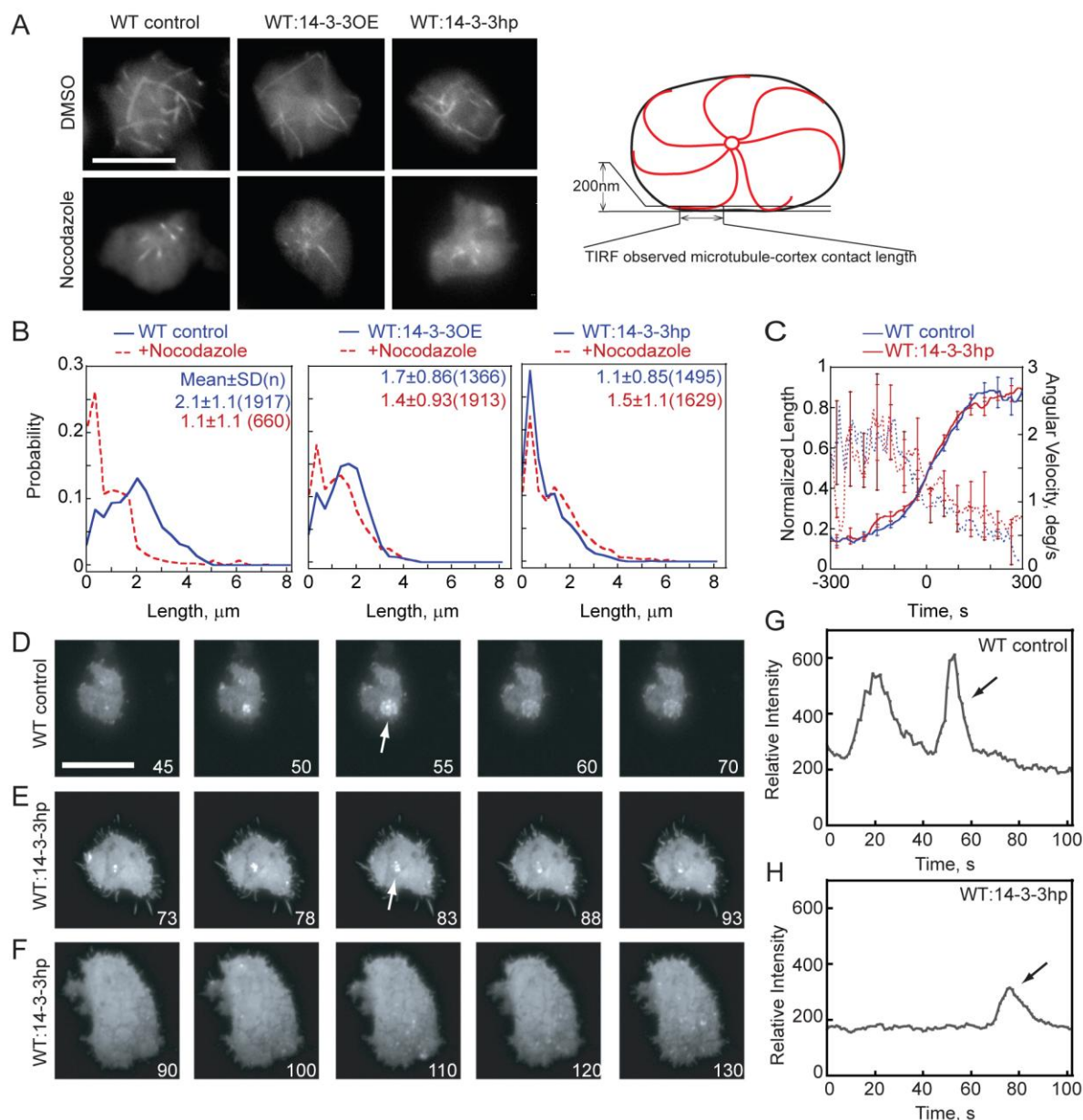


**Figure S3. 14-3-3 Controls Cell Cortex Function, Including Microtubule-Cortex Interactions**

(A) Microtubule contacting the cell cortex were imaged by TIRF microscopy. Cartoon illustrates the microtubule-cortex contact observed by TIRF imaging. Scale bar, 5  $\mu$ m.

(B) The probability distributions of the microtubule-cortex contact length for wild type control, WT:14-3-3OE, and WT:14-3-3hp with and without nocodazole treatment are shown. The mean $\pm$ SD and the total number (n) of analyzed microtubule-cortex contact events are provided on each graph. With the exception of WT:14-3-3OE+Nocodazole compared to WT:14-3-3hp+Nocodazole, all distributions are significantly different (MW:  $p < 0.01$  with some  $p$ -values were several orders of magnitude less than 0.01).

(C) Quantitative analysis of mitotic spindle dynamics of wild type control (n=12) cells and WT:14-3-3hp (n=21) cells showed no differences in the rate of spindle elongation (solid lines, left axis) or angular velocity (dotted lines, right axis). Error bars represent standard error of the mean.

(D) Time series collected using TIRF imaging of a WT control cell, expressing GFP-LimE $\Delta$ coil, shows that these cells generate actin waves. The wave marked with a white arrow corresponds with the peak in panel G.

(E and F) Time series collected by TIRF imaging of two 14-3-3hp cells, expressing GFP-LimE $\Delta$ coil, shows that these cells seldom form actin waves. The cell shown in E forms a wave (marked with white arrow, which corresponds with the peak in panel H below), whereas the cell in F does not exhibit any wave activity.

(G) Fluorescence intensity plot vs. time of the wave marked in panel D.

(H) Fluorescence intensity plot vs. time of the wave marked in panel E. For G and H, black arrows mark the peak with the corresponding wave shown in the images. Full quantitative analysis of wave properties can be found in Table S2.

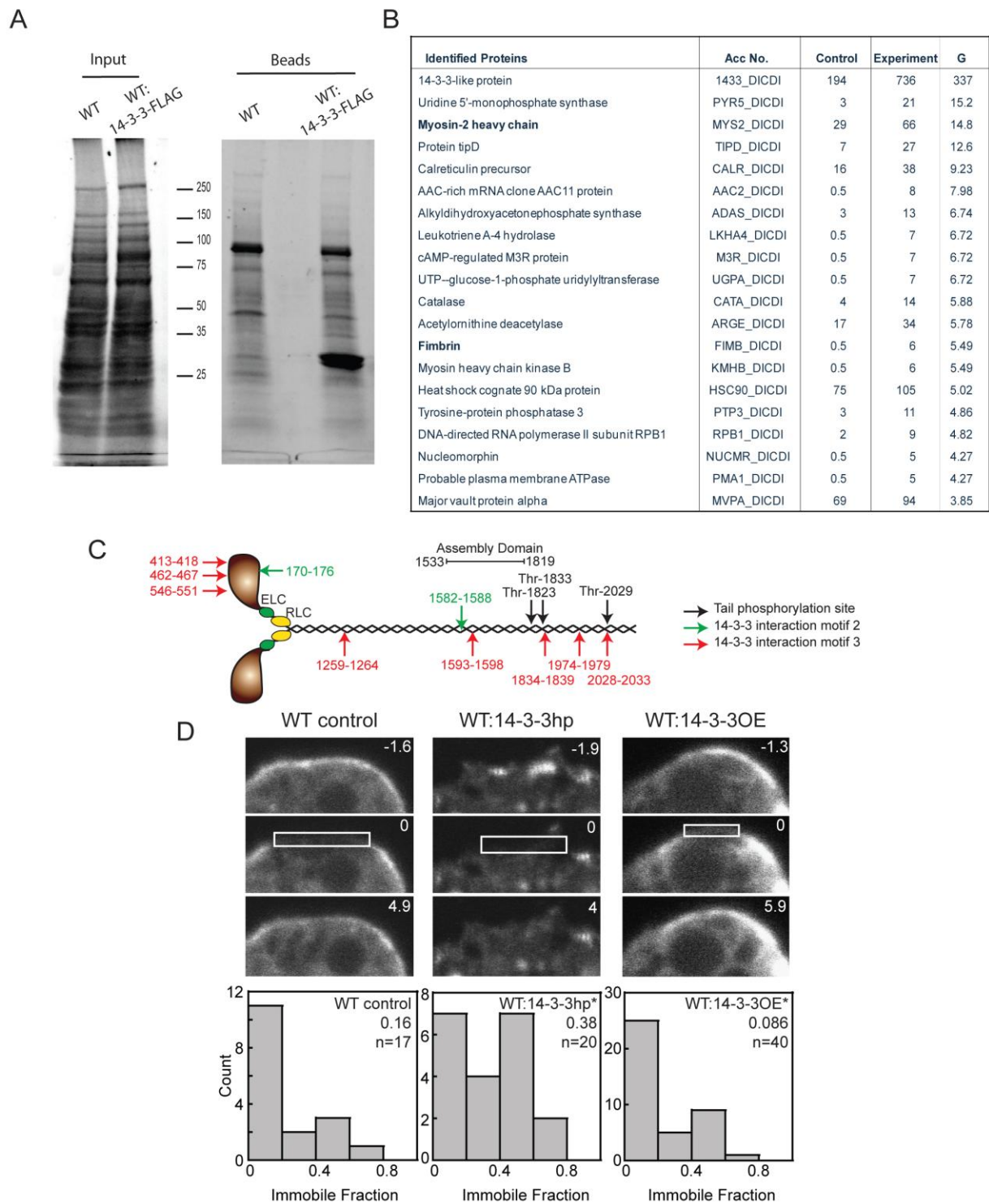


Figure S4.

#### **Figure S4. 14-3-3 Interacts with Myosin II**

(A) Coomassie stained gels of soluble input material and the proteins eluted from the anti-FLAG resin, using FLAG peptide. Input materials were derived from wild type cells versus WT cells expressing 14-3-3-FLAG protein.

(B) The list of potential binding partners after LC-MS analysis. Protein name, genome accession identifier, counts in the control vs. the experimental (14-3-3-FLAG) sample and the statistical parameter G are provided. Myosin II heavy chain is third on the list as one of the most significant hits.

(C) Cartoon diagram identifying the consensus 14-3-3 motif 2 and motif 3 binding sites. No motif 1 consensus sites were found. Three motif 3 sites are found flanking or overlapping with the three critical threonines that are the major substrates of myosin heavy chain kinases. Phosphorylation of these three threonines locks the myosin heavy chain into an assembly incompetent state and/or helps drive the myosin heavy chain monomer out of the bipolar thick filament. The 14-3-3-consensus-binding sites were identified using ELM (<http://elm.eu.org>).

(D) FRAP analysis shows that 14-3-3hp increases the immobile fraction of GFP-myosin II. Numbers in the images are time in seconds. Time 0 is the first frame after photobleaching. Frequency histograms show the distributions of immobile fractions (medians and sample sizes listed). Wild type is intermediate between the WT:14-3-3hp and WT:14-3-3OE cells, whereas WT:14-3-3OE is significantly different than WT:14-3-3hp (MW:  $p=0.015$ )

**Table S1. Strains Used in This Study**

Strain	Genotype	Experimental Applications
WT control	Ax3(Rep orf+): pLD1A15SN	cDNA library screen, MPA, Western, immunocytochemistry, dividing trajectory, DAPI staining
WT:14-3-3OE	Ax3(Rep orf+): pLD1A15SN:14-3-3	MPA, Western, immunocytochemistry
WT:14-3-3-GFP	Ax3(Rep orf+): pLD1A15SN:14-3-3-GFP	3D-decon, Western, TIRF, MPA
WT:14-3-3(K49E)-GFP	Ax3(Rep orf+): pLD1A15SN:14-3-3(K49E)-GFP	3D-decon, MPA
WT:GFP	Ax3(Rep orf+): pLD1A15SN:GFP	3D-decon
WT:14-3-3hp	Ax3(Rep orf+): pLD1A15SN:14-3-3 RNAi	Suspension culture, MPA, Western, dividing trajectory, DAPI staining, immunocytochemistry
<i>RacE</i> control	$\Delta$ <i>RacE</i> : pLD1A15SN	3D-decon, suspension culture, MPA, dividing trajectory
<i>RacE</i> :14-3-3-GFP	$\Delta$ <i>RacE</i> : pLD1A15SN:14-3-3-GFP	3D-decon
<i>RacE</i> control: 14-3-3-GFP	$\Delta$ <i>RacE</i> : pLD1A15SN:14-3-3-GFP; pDRH	3D-decon
<i>RacE</i> :14-3-3-GFP; mCh-RacE	$\Delta$ <i>RacE</i> : pLD1A15SN:14-3-3-GFP; pDRH:mCh-RacE	3D-decon
<i>RacE</i> :14-3-3OE	$\Delta$ <i>RacE</i> : pLD1A15SN:14-3-3	Suspension culture, MPA, dividing trajectory
<i>RacE</i> <sup>24E</sup> control	<i>RacE</i> <sup>24E</sup> : pLD1A15SN	Suspension culture, fractionation
<i>RacE</i> <sup>24E</sup> :14-3-3OE	<i>RacE</i> <sup>24E</sup> : pLD1A15SN:14-3-3	Suspension culture
<i>RacE</i> <sup>24E</sup> :GFP-RacE	<i>RacE</i> <sup>24E</sup> : pLD1A15SN:GFP-RacE	Suspension culture, fractionation
WT control: GFP-tub	Ax3(Rep orf+): pDRH:GFP-tub; pLD1A15SN	Microtubule imaging, TIRF, 3D-decon
WT:14-3-3OE; GFP-tub	Ax3(Rep orf+): pDRH:GFP-tub; pLD1A15SN:14-3-3	Microtubule imaging, TIRF, 3D-decon
WT:14-3-3hp; GFP-tub	Ax3(Rep orf+): pDRH:GFP-tub; pLD1A15SN:14-3-3hp	Microtubule imaging, TIRF, 3D-decon
WT control:GFP-limE $\Delta$ coil	Ax3(Rep orf+): pLD1A15SN; pDRH:GFP-limE $\Delta$ coil	Actin wave analysis, TIRF, Western
WT: 14-3-3hp; GFP-limE $\Delta$ coil	Ax3(Rep orf+): pLD1A15SN:14-3-3hp; pDRH:GFP-limE $\Delta$ coil	Actin wave analysis, TIRF, Western
WT:14-3-3-FLAG	Ax3(Rep orf+): pLD1A15SN:14-3-3-FLAG	LC-MS analysis
<i>cortl</i> <sup>1151</sup> control	<i>cortl</i> <sup>1151</sup> (HS1151):pLD1A15SN	Suspension culture
<i>cortl</i> <sup>1151</sup> :Enl-tr	<i>cortl</i> <sup>1151</sup> (HS1151):pLD1A15SN:Enl-tr	Suspension culture
<i>cortl</i> <sup>1151</sup> :14-3-3OE	<i>cortl</i> <sup>1151</sup> (HS1151):pLD1A15SN:14-3-3OE	Suspension culture
<i>myoll</i> : GFPmyoll	<i>mhcA</i> (HS1): pDRH:GFPmyoll; pLD1A15SN	Myosin II quantification, FRAP
<i>myoll</i> : GFPmyoll; 14-3-3hp	<i>mhcA</i> (HS1): pDRH:GFPmyoll; pLD1A15SN:14-3-3hp	Myosin II quantification, FRAP
<i>myoll</i> : GFPmyoll; 14-3-3OE	<i>mhcA</i> (HS1): pDRH:GFPmyoll; pLD1A15SN:14-3-3OE	Myosin II quantification, FRAP
<i>myoll</i> : mCherry-myoll	<i>mhcA</i> (HS1): mCh-myoll:pDRH	Immunocytochemistry, myosin II purification
<i>myoll</i> control	<i>mhcA</i> (HS1) with or without pLD1A15SN	Immunocytochemistry, MPA
<i>myoll</i> :14-3-3OE	<i>mhcA</i> (HS1): pLD1A15SN:14-3-3OE	MPA
<i>myoll</i> :14-3-3-GFP	<i>mhcA</i> (HS1): pLD1A15SN:14-3-3-GFP	MPA, Imaging



**Table S2. Summary of Wave Statistics**

Strain	Percentage of cells with waves ( $\pm$ SE; n) <sup>a</sup>	Waves/cell/min (n=number of waves) <sup>b</sup>	Waves/ $\mu\text{m}^2/\text{min}^b$	Wave Velocity ( $\mu\text{m}/\text{min}$ ) <sup>b,c</sup>	Normalized Wave Amplitude <sup>b</sup>	Wave Width Time (s) <sup>b</sup>
WT control	100% ( $\pm$ 0%; 22)	1.7 $\pm$ 0.20 (105)	0.019 $\pm$ 0.0043	7.0 $\pm$ 0.19	2.3 $\pm$ 0.082	21 $\pm$ 0.59
WT:14-3-3hp	53% ( $\pm$ 13%; 15)	1.1 $\pm$ 0.31 (16)	0.015 $\pm$ 0.0065	8.8 $\pm$ 0.58	2.2 $\pm$ 0.20	19 $\pm$ 1.3

<sup>a</sup>Standard errors calculated as  $\text{SE} = \sqrt{f(1-f)/n}$  where f is the fraction of responders; CP:  $z=2.91$ ;  $p=0.0036$

<sup>b</sup>Values are derived from cells that produced waves.

<sup>c</sup>ST:  $p<0.01$ .